

Diagenesis of Magnetic Minerals in Active/Relict Methane Seep: Constraints from Rock Magnetism and Mineralogical Records from Bay of Bengal

Virsen Gaikwad^{1,2}, Firoz Badesab^{1*}, Pawan Dewangan¹, Mahender Kotha²

¹ CSIR - National Institute of Oceanography, Dona Paula 403004, Goa, India

²School of Earth Ocean and Atmospheric sciences, Goa University 403206, Goa, India

*Correspondence: Firoz Badesab (firoz@nio.org)

Abstract

In this study, we conducted a comprehensive investigation of rock magnetic, mineralogical, and sedimentological records of sediment cores supplemented by a high resolution seismic data to elucidate the controls of structural and diagenetic (*early versus late*) processes on the sediment magnetism in active and relict cold seep sites in the Bay of Bengal. Two distinct sediment magnetic zones (Z-I and Z-II) are defined based on the down-core variations in rock magnetic properties. The sediment magnetism is carried by complex magnetic mineral assemblages of detrital (titanomagnetite, titanohematite) and authigenic (fine-grained greigite) minerals. Overall, the magnetic susceptibility varies over one order of magnitude with highest values found in relict core. Uppermost sediment magnetic zone (Z-I) is characterized by higher concentration of magnetite as seen through elevated values of magnetic susceptibility (χ_{lf}) and saturation isothermal remanent magnetization (SIRM). A systematic gradual decrease of χ_{lf} and IRM_{1T} in Z-I is attributed to the progressive diagenetic dissolution of iron oxides and subsequent precipitation of iron sulfides. Magnetic grain size diagnostic (ARM/ IRM_{1T}) parameter decreases initially due to the preferential dissolution of fine-grained magnetite in the sulfidic zone (Z-I), and increases later in response to the authigenic formation of magnetite and greigite in methanic zone (Z-II). Distinct low S-ratio and χ_{lf} values in methanic zone of relict core is due to increased relative contribution from highly preserved coercive magnetic (titanohematite) grains of detrital origin which survived in the diagenetic processes. A strong linkage between occurrence of authigenic carbonates and greigite formation is observed. Two plausible mechanisms are proposed to explain the formation and preservation of greigite in Z-I and Z-II: (a) decline in methane flux due to massive hydrate accumulation within the active fault system and formation of authigenic carbonate crust in the sub-surface sediments hindered the supply of upward migrating fluid/gas; thereby limiting the sulfide production which preferentially enhanced greigite formation in Z-I and (b) restricted supply of downward diffusing sulfide by the carbonate layers in the uppermost sediments created a sulfide deficient zone which inhibited the pyritization and favoured the formation of greigite in the methanic zone (Z-II).

Key words: Cold seep, Methane hydrate, Rock magnetism, Diagenesis, Bay of Bengal

Introduction

At active cold seeps, methane and hydrogen sulfide fluids emanate from the seafloor. These fluids led to diagenesis of magnetic minerals at or below the sediment-water interface, wherein primary detrital iron-bearing magnetic minerals undergoes reductive dissolution and are converted into iron sulfides e.g., greigite, pyrrhotite, pyrite (Amiel et al., 2020; Boetius et al., 2000; Canfield and Berner, 1987; Dewangan et al., 2013; Jørgensen et al., 2004; Lin et al., 2017; Kars and Kodama 2015; Riedinger et al., 2005; Roberts, 2015; Rodelli et al., 2018; Rowan et al., 2009; Suess, 2014). Rock magnetic properties of methanic sediments from active cold seep and gas hydrate dominated sedimentary systems have been extensively studied to understand the magnetic mineral diagenesis. For example in Nankai trough, Japan (Kars and Kodama, 2015), Cascadia Margin (Housen and Musgrave, 1996; Larrasoña et al., 2007), continental margin offshore of south-western Taiwan (Horng and Chen, 2006), continental margin off Argentina and Uruguay (Riedinger et al., 2005), Bay of Bengal (Badesab et al., 2017; 2019, 2020a,b,c), Southern Eastern Mediterranean continental shelf (Amiel et al., 2020), Niger deep-sea fan (Dillon and Bleil, 2006), Bulls eye vent off Vancouver Island, Canada (Novosel et al., 2005), and North-western Weddell Sea (Reilly et al., 2020).

Structural control on methane seepage at cold seep sites has been well reported using high resolution seismic and bathymetry data. For example Lomvi pockmark, Vestnesa Ridge, offshore Svalbard (Berndt et al., 2014; Bünz et al., 2012; Yao et al., 2019), Harstad Basin, southwest Barents Sea (Crémière et al., 2018), Bay of Bengal (Dewangan et al., 2020), Concepción Methane Seep Area, offshore Central Chile (Geersen et al., 2016), Taixinan Basin, South China Sea (Wang, et al., 2018) Central Nile deep sea fan (Römer et al., 2014), Nankai accretionary prism (Henry et al., 2002), Congo basin (Wenau et al., 2015) and Black Sea (Bohrmann et al., 2003). Extensive geological and geophysical studies established the presence of fracture-filled and massive-type gas hydrate deposits in the Krishna-Godavari (K-G) basin (Collett et al., 2008; Dewangan et al., 2010; Dewangan et al., 2011; Kumar et al., 2014; Shankar and Riedel, 2010). Fractures/faults, generated from shale-tectonism, provide an efficient gas plumbing system in the K-G basin (Dewangan et al., 2010). Fluid migration through these fractures/faults led to the occurrence of paleo-cold seeps in the K-G basin (Dewangan et al., 2010; Mazumdar et al., 2009). In some active faults, methane migrates up to the seafloor and form active/relict cold seep system associated with shallow gas hydrates (Gullapalli et al., 2019; Mazumdar et al., 2019; Figure 1).

Methane migrates from deep-seated gas reservoirs and interacts with downward diffusing seawater sulfate to trigger multiple zones of anaerobic oxidation of methane (AOM) (Jørgensen et al., 2004; Knittel and Boetius, 2009; Lin et al., 2018) driven by sulfate reduction (Mazumdar et al., 2019). At

seep sites, non-steady and multiple diagenetic fronts would yield a complex pattern of magnetic mineral assemblages (Reilly et al., 2020; Roberts, 2015). Recent study by Reilly et al. (2020) provides new insights on magnetic mineral diagenesis through a shallow sulfate-methane transition zone (SMTZ) in a sediment core from Perseverance Drift, Northwestern Weddell Sea, Antarctica. They reported that non-steady state disturbances including fluctuations in carbon flux and sedimentation can shift the pore-water geochemical profiles resulting in preservation of authigenic ferrimagnetic iron sulfides. In contrast, steady-state diagenetic processes at relict sites would lead to dissolution of detrital magnetic minerals followed by subsequent diagenetic formation of iron sulfide (pyrite) which can significantly reduce magnetic susceptibility of the bulk sediments (Amiel et al., 2020; Canfield and Berner, 1987; Kars and Kodama, 2015; Mohamed et al., 2011; Reilly et al., 2020; Roberts et al., 2005; Roberts, 2015; Roberts and Weaver, 2005, Lin et al., 2020).

Magnetic minerals are potential recorders of the geological and methane-related geochemical processes and provide vital information on the methane seepage dynamics and diagenetic processes in marine gas hydrate sedimentary system (Badesab et al., 2019; Kars and Kodama, 2015; Larrasoana et al., 2007; Musgrave et al., 2006; Roberts, 2015). Previous rock magnetic studies on sediment cores overlying shallow and deep-seated gas hydrate deposits in the K-G basin mainly aimed at delineating the magnetic signatures of detrital and diagenetic processes associated with evolution of gas-hydrate system (Badesab et al., 2017; Dewangan et al., 2013). For example, a magnetic based proxy for deciphering paleo-methane seepage events and sediment dispersal patterns, tracking of the rapid sedimentation events and its control on the magnetic mineral diagenesis and evolution of gas hydrate deposits was developed (Badesab et al., 2017; 2019; 2020b; Usapkar et al., 2014). Furthermore, the mechanism of formation and preservation of greigite in deep methanic sediments were unravelled by Badesab et al., 2020c. The occurrence of silicate-hosted greigite inclusion were reported by Badesab et al., 2020a. They further highlighted its importance in understanding magnetic mineral diagenesis in the gas hydrate system. More recently, Badesab et al., (2020c) conducted a comprehensive rock magnetic and mineralogical investigation on a seep-impacted sediment core from a newly discovered site and successfully delineated the processes governing the methane seepage dynamics and evolution of shallow gas hydrate (2-3 mbsf) system in the K-G basin. However, a dedicated rock magnetic study focussing on understanding the complex diagenetic (early and late) processes controlled by variability in methane fluxes and underlying fault/fractures at active and relict seep dominated sedimentary systems is still lacking.

Sediment cores retrieved during gas hydrate discovery cruise in 2018 in the K-G basin provides an excellent opportunity to establish a magnetic mineral inventory and investigate the diagenetic

processes at active/relict and paleo-seep sites associated with shallow and deep-seated marine gas hydrates respectively. The active seep sites (SPC-01 to SPC-06) are mainly characterized by gas flares as observed in the water-column images, higher methane flux and presence of live chemosynthesis dependent organisms predominantly Bivalvia, Gastropods, and Polychaete (Dewangan et al., 2020; Mazumdar et al., 2019). Relict seep site (Stn-11/GC-02) is characterized by the absence of gas flares, presence of non-living shell fragment, *Calyptogena* Sp. and occurrence light brown colored authigenic carbonates at 48 cm below sea floor at this site. Contrastingly, paleo-seep site (MD161/Stn-8) is marked by the presence of methane-derived carbonates, non-living with chemosynthetic clams (*Calyptogena* sp.) and authigenic carbonates within 17-23 mbsf in this core which provided evidence of seepage of methane and sulfide-bearing fluids to the seafloor in the geological past (Mazumdar et al., 2009). In this study, we conducted a comprehensive investigation of rock magnetic, mineralogical, and sedimentological records of sediment cores supplemented by high resolution seismic data to elucidate the controls of structural and diagenetic (*early versus late*) processes on the sediment magnetism in an active (SSD-45/Stn-4/SPC-01 to SPC-06) and relict (SSD-45/Stn-11/GC-02) cold seep sites in the Bay of Bengal.

Geology Of Krishna-Godavari Basin

Krishna-Godavari (K-G) basin is situated along the eastern continental margin of India (Figure 1). The K-G basin covers onshore area of 28,000 km² and offshore area about 145,000 km² and extends from Ongole in South to Vishakhapatnam in north (Ohja and Dubey, 2006). Average sediment thickness is about 3-5 km in onshore region, which increases to about 8 km in the offshore region (Bastia, 2007; Prabhakar and Zutshi, 1993). The Krishna and Godavari rivers and their tributaries deliver major sediment load to the K-G basin. Annual sediment load delivered by the Krishna and Godavari rivers is estimated to be around 67.7×10^6 and 170×10^6 metric ton respectively (Biksham and Subramanian, 1988; Ramesh and Subramanian, 1988). Both the river systems flows through the Deccan trap basalt and Precambrian metamorphic rocks and supplies large amount of detrital magnetite-rich sediments to the K-G basin (Ramesh and Subramanian 1988; Sangode et al., 2007). Sediments in the K-G basin are primarily composed of montmorillonite clay with traces of illite and kaolinite (Rao, 1991). Neo-tectonic activities in the K-G basin resulted in the formation of geomorphic structures including shale diapirs, mounds, and faults. Migration of methane through the fault system favoured the accumulation of gas hydrates in the K-G basin (Dewangan et al., 2010)

Methodology

Sampling and measurements

During gas hydrate exploration cruise (SSD-45) of Council of Scientific and Industrial Research - National Institute of Oceanography (CSIR-NIO) onboard R/V Sindhu Sadhana, six short spade cores (SPC-01 to SPC-06; Table. 1) were retrieved from active site (SSD-45/Stn-4) and one gravity core (Stn-11/GC-02) from relict seep site (as evident through the presence of non-living shell fragment, *Calypptogena* Sp. and authigenic carbonates at 48 cmbsf in this core) in the K-G basin (Figure 1). Upon recovery, sediment cores from active sites smelled strongly of hydrogen sulfide (H₂S) suggesting a shallow SMTZ that motivated this study. Magnetic samples were taken onboard immediately after collection of pore water samples to minimize sediment alteration due to warmer temperatures and oxygen exposure. The cores were sub-sampled in the presence of high purity nitrogen flushing to minimize the exposure of samples to atmospheric conditions, which could oxidize hydrogen sulfide or iron mono-sulfide. Samples for magnetic analysis were collected by pushing non-magnetic plastic bottles into the split halves at ~ 2 cm intervals. After sub-sampling, magnetic samples were transferred to a cold room (4°C) for storage. Magnetic measurements were carried out on wet sediment samples (packed in 25 mm plastic sample bottled) at the Paleomagnetic laboratory of CSIR-NIO and specialized rock magnetic measurements on dry samples at Center for Advanced Marine Core Research (CMCR), Kochi University, Japan.

Magnetic measurements

Low-field magnetic susceptibility measurements were carried out using a Bartington Instruments MS2B dual frequency susceptibility meter. The susceptibility was measured at low (lf) and high (hf) frequencies $\chi_{lf} = 0.47$ kHz and $\chi_{hf} = 4.7$ kHz. The frequency-dependent susceptibility was calculated as $\chi_{fd} \% = (\chi_{lf} - \chi_{hf})/\chi_{lf} \times 100\%$. All remanent magnetizations were measured using an AGICO JR-6A spinner magnetometer. An anhysteretic remanent magnetization (ARM) was imparted using a 100 mT alternating magnetic field superimposed on a fixed direct current (DC) bias field of 50 μ T. An isothermal remanent magnetization (IRM) was imparted using an inducing field of +1T in the forward direction by a MMPM10 pulse magnetizer. S-ratio is calculated as the ratio of IRM at -300mT and SIRM (IRM_{-300mT}/IRM_{1T}) (Thompson and Oldfield, 1986). Thermomagnetic measurements were conducted on eight selected samples using a Natsuhara Giken (Model NMB-89) magnetic balance at CMCR with a heating rate of 10 °C/min in a 0.3-T field.

Hysteresis loops, first-order reversal curves (FORC) (Pike et al., 1999), and back-field curves were also measured for fourteen selected samples with a maximum field of 1 T (number of loops per

FORC: 91, averaging time: 200 ms, field increment: 4 mT, and a slew rate limit: 1T/s) at CMCR. Processing of FORC diagrams were done using the FORCinel software (Harrison and Feinberg, 2008). FORC distributions were processed using a smoothing factor (SF) of 5, but SF = 6 were used where possible. Low-temperature magnetic measurements were conducted on selected samples using a Quantum Design Magnetic Properties Measurement System (MPMS) at CMCR. A room temperature SIRM (RT-SIRM) was imparted at room temperature (300 K) in 2.5 T. Samples were then cooled to 5 K and warmed back to 300 K in a zero magnetic field. A low temperature SIRM (LT-SIRM) was then imparted at 5 K in 2.5 T. Samples were warmed up to 300 K in a zero magnetic field (termed “ZFC” for zero field-cooled). Samples were then cooled to 5 K in the presence of a 2.5 T magnetic field. A LT-SIRM was again imparted at 5 K, and samples were warmed to 300 K in a zero magnetic field (termed “FC” for field-cooled).

Bulk sediment grain size analyses

Sediment grain size measurements were carried out using a Malvern Mastersizer 2000 Laser Particle Size Analyzer at CSIR-NIO. Before analyses, desalination of sediment samples were carried out by washing repeatedly with deionized water followed by decarbonisation using dilute HCl (1N) acid. For removal of organic carbon, samples were treated with 10% H₂O₂ and later, Sodium hexametaphosphate was added to sediments for better dispersal of the sediment fractions. Grain size values are reported as volume%.

Mineralogical analysis

Magnetic particles were extracted from bulk sediments following the separation method of Petersen et al. (1986). Bulk sediment samples were disintegrated into 500 ml of distilled water with addition of 200 mg of a dispersing agent (sodium hexametaphosphate) and suspensions were treated with ultrasonics. Further, sediment suspension was allowed to continuously flow through the magnetic extraction set-up. The extraction method is based on the principle that high magnetic field gradients are created by inserting magnets on the teflon coated magnetic finger. During continuous circulation, magnetic particles within the bulk sediments get attracted towards the magnetic finger. These magnetic fractions are removed and washed several times in a small volume of distilled water to remove clay fractions and other contaminants. Magnetic particles were mounted on a carbon tape and were carbon coated for imaging. Images of magnetic grains were captured in secondary electron (SE) imaging mode at energy levels between 15 and 20 keV using a scanning electron microscope (SEM; JEOL JSM-5800 LV) at CSIR-NIO. Energy dispersive X-ray spectroscopy (EDS) probe attached to the microscope was used to determine the composition of magnetic minerals. Magnetic

mineralogy was determined on the extracted magnetic particles using a Rigaku X-Ray Diffractometer (Ultima IV). The samples were allowed to run from 15° to 65° of 2 θ at 1°/min scan speed using Cu K α radiation ($\lambda = 1.5414 \text{ \AA}$).

Results

Down-Core Changes in Rock magnetic Parameters

The magnetic susceptibility (χ_{f}) profile of all spade cores (SPC-01 to SPC-06) from active seep and a gravity core from relict (SSD-45/Stn-11/GC-02) sites along with IRM_{1T}, ARM/IRM_{1T}, IRM_{1T}/ χ_{f} and S-ratio are shown in Figure 2. Two distinct sediment magnetic zones (Z-I and Z-II) are defined based on down-core variations of χ_{f} in all cores (Figures 2A, G, M, S, Y, A5, A11). In active methane-seep influenced sediment cores, Z-I is marked by relatively higher values of χ_{f} and IRM_{1T} indicating high concentration of magnetic minerals as compared to that observed in Z-II. Magnetic grain size diagnostic proxy (ARM/IRM_{1T}) showed variations in Z-I and Z-II of all analyzed sediment cores (Figure 2; Maher and Thompson, 1999; Peters and Dekkers, 2003). A general trend of downcore decrease suggesting coarsening in magnetic grain size is observed till the bottom of Z-I in all cores except SPC-02 (Figure 2I). In SPC-01, SPC-03, SPC-04, SPC-06, and GC-02 ARM/IRM_{1T} first decreases probably due to preferential dissolution of fine-grained magnetite in Z-I, and rises downcore in response to the authigenic formation of greigite (Figures 2C, O, U, A7, A13) or fine-grained magnetite (Lin et al., 2020; Rodelli et al., 2019) in Z-II. A mixed trend of ARM/IRM_{1T} in SPC-02 and SPC-05 reflects the dominance of both fine and coarse magnetic particles in Z-II (Figures 2I, A1). Two distinct patterns in grain size indicator of magnetic iron sulfides (IRM_{1T}/ χ_{f}) are observed (Figure 2; Maher and Thompson, 1999; Peters and Dekkers, 2003; Snowball, 1991; Snowball and Thompson, 1990). A trend of initial rise in IRM_{1T}/ χ_{f} values are noticed in Z-I of cores SPC-01, SPC-02, SPC-03, SPC-05, and GC-02 suggest the presence of fine grained magnetic particles (Figures 2D, J, P, A2). After initial rise, a gradual decline in IRM_{1T}/ χ_{f} values till end of Z-II of the same cores is noticed (Figures 2D, J, P, A2, A14). Overall, S-ratios vary between 0.82 and 0.99 for majority of the samples suggesting that bulk magnetic mineralogy is characterized by both soft as well as hard coercive minerals in the cores from active seep sites (Figures 2E, K, Q, W, A3, A9; Frank and Nowaczyk, 2008). A systematic downcore decrease in χ_{fd} (%) is seen in all cores from active sites (Figures 2F, L, R, X, A4, A10). High values in Z-I indicate higher concentration of fine-grained magnetic particles, while relatively lower values in Z-II suggest the relative dominance of coarse magnetic particles. Interestingly, we noticed an opposite trend in χ_{fd} (%) profile of relict site. Lower χ_{fd} (%) values were found in Z-I and vice-versa (Figure 2A16).

Magnetic record of relict site (SSD-45/Stn-11/GC-02) showed similar magnetic zonation (Z-I, Z-II), but exhibit different downcore trends in ARM/IRM_{1T}, IRM_{1T}/ χ_{lf} and S-ratio (Figures 2A11-A16). Three sediment intervals (11 cmbsf, 13 cmbsf, 15 cmbsf) within Z-I showed higher χ_{lf} , IRM_{1T} and IRM_{1T}/ χ_{lf} suggesting the presence of fine-grained ferrimagnetic iron sulfides in these samples (Figures 2A11, A12, A14). An anomalous increase in ARM/IRM_{1T} between 39 – 57 cmbsf suggests the dominance of fine-grained magnetic particles in this interval (Figure 2A13). A major shift in S-ratio at 29 cmbsf followed by a minor rise in IRM_{1T} downcore (29 – 33 cmbsf) indicates that the relict site has much higher concentration of high-coercive (coarse-grained) minerals (Figures 2A12, A15) as compared to other sites.

Magnetic Mineralogy and Grain Size Diagnostic Parameters

Thermomagnetic Measurements

Figures 3A-H show the thermomagnetic curves of the representative sediment samples from Z-I and Z-II of cores SPC-01/02/03/05. A steady decrease in χ between 552°C and 633°C in majority of the samples imply that the bulk magnetic mineralogy is governed by magnetite (Dunlop et al., 1997). Two samples from SPC-01(21 cmbsf) (Figure 3B) and SPC-02 (41 cmbsf) (Figure 3D) showed a major drop in χ at 695°C and 673°C respectively. A minor increase in χ between 357°C and 473°C for most of the samples could be either due to the presence of titanomagnetite with a wide range of Ti-contents (Lattard et al., 2006) or because of conversion of paramagnetic minerals into magnetite during heating process (Hirt and Gehring, 1991; Pan et al., 2000; Passier et al., 2001; Figures 3A-H).

FORC diagrams

FORC diagram provided additional information on the type of magnetic minerals and their domain states. Representative FORC diagrams for Z-I and Z-II samples of cores SPC-01/02/03/06 are shown in Figures 4A-N. In majority of the samples, FORC distributions are characterized by closed contours with a peak at B_c ~ 10 – 12 mT which suggest that magnetic particles exhibit vortex state to multidomain (MD) type behavior (Figures 4A–N; Lascau et al., 2018; Roberts et al., 2000; Roberts et al., 2017)

Low-Temperature Measurements

Results of the low-temperature magnetic measurements displaying characteristic magnetic signatures with respect to the sediment magnetic zones (Z-I, Z-II) (Figure 5). A typical Verwey transition (T_v) temperature indicative of presence of magnetite (Figures 5A,B,D,E,F) is noticed in RT-SIRM, ZFC-FC, and in the first derivative of magnetization curves (Chang et al., 2016; Özdemir et al., 2002; Verwey, 1939,1947). Samples from magnetically reduced zone (Z-II) do not exhibit any T_v. The

displayed LT magnetization curve (Figure 5C) at 29 cmbsf of core SPC-01 is indicative of maghemite (Özdemir and Dunlop, 2010). Approximately 62% loss of RT-SIRM induced at 5K is seen during warming between 5 and 30 k (Figure 5C) indicating the presence of SP size magnetic particles. We do not observe any Besnus transition (typical for pyrrhotite; Besnus and Meyer, 1964; Dekkers, 1989; Larrasoña et al., 2007) in the studied samples.

Identification of Magnetic Mineralogy using X-ray Diffraction Analysis and Scanning Electron Microscopy

Titanomagnetite and greigite are the dominant magnetic minerals identified in all the sediment magnetic zones (Figures 6A-M). Greigite is present in both magnetic zones (Z-I and Z-II) of the cores SPC-01 (Figures 6B, C), SPC-02 (Figures 6E, F), and SPC-04 (Figures 6J, K). The electron microscopic images and respective EDS spectra of magnetic particles extracted from different sediment depth intervals of spade cores SPC-01-04 are presented in Figures 7A-L. Ferrimagnetic iron oxides (detrital) and sulfides (diagenetic) minerals of different sizes and shapes are identified in all spade cores (Figures 7A-L). Well-preserved (Figures 7A, D, G, I) as well as diagenetically altered (Figures 7C, H) titanomagnetite grains are found in both sediment magnetic zones. EDS data for these grains indicate the presence of titanium, iron, and oxygen with minor amount of silicon, aluminium, calcium, potassium, manganese and magnesium. Numerous diagenetically formed iron sulfides occurring as framboidal crystals and individual grains are observed (Figures 7B, K, L) and EDS data indicate the presence of sulfur and iron along with minor amounts of aluminium and silicon (Figures 7A-L). Greigite was found to occur as fine-grained minerals only in few samples and the EDS results of these grains show the presence of sulfur and iron with minor traces of calcium, potassium, silicon, aluminium, and magnesium (Figures 7E, F, J). The titanomagnetite grains in Figure 7C and 7L show a shrinkage-cracks typical of low-temperature maghemitization (Nowaczyk, 2011). The cracks on the grains most likely indicate the areas where dissolution might have started. In the relict seep core (GC-02), magnetic mineralogy is carried by titanomagnetite, titanohematite and greigite particles (Figures 9I-P). Z-I is dominated by coarse-grained titanomagnetite and titanohematite grains. A skeletal type titanohematite grains exhibiting the dissolution features are observed in Z-I (Figure 9J) and Z-II (Figures 9M, O, P). Numerous titanomagnetite grains showing the overgrowth of fine-grained greigite particles are noticed in Z-I (Figures 9K, L) and Z-II (Figure 9O).

Grain Size Distributions of Sediments, Chemosynthetic Communities and Authigenic Carbonates

Bulk sediment grain size in the studied cores mainly composed of silt and clay size fractions (Figure 8). Sand content is relatively low and varies between 0.99 to 18.58 vol%. Sand bearing sediment layers are observed throughout the core only in SPC-04/05/06 (Figures 8D-F). Higher magnetic susceptibility was found only in silt and clay size fractions (Figures 8A-F). Characteristic chemosynthetic living communities (Mazumdar et al., 2019) including *Bathymodiolus* sp., (Figures 9A, B, C, E), *Acharax* sp. shell (Figure 9F) and Decapod crustaceans (squat lobsters) belonging to the family Galatheidae and Munidopsidae (Figure 9D) are abundantly found at the active methane seep sites. At relict seep site (SSD-45/Stn-11/GC-02), light brown colored authigenic carbonates showing various morphologies and a non-living shell fragments (*Calypdogena* sp.) were found at 48 cmbsf (Z-II) in this core (Figures 9G and H).

Correlation between magnetic parameters of active and relict methane-seep sites

A clear distinction in terms of magnetic mineral concentration, grain size and mineralogy is seen between active and relict seep sites (Figure 10). A positive correlation between χ_{lf} and IRM_{IT} is observed in all the samples, but showed different slopes which can be attributed to the presence of different magnetic mineralogies (Figure 10A). Contrastingly, anomalous lower values (0.11 - 0.55) of S-ratio and wide range of χ_{lf} displayed by samples from relict site indicates the predominance of highly coercive minerals (Figure 10C). Coupling between magnetic grain size (ARM/IRM_{IT}) and physical grain size is noticed in majority of samples from active and relict seep sites (Figure 10D). We observed two populations (A and B). The samples from group-A showed uniformity in physical grain size, but exhibit wide range of magnetic grain size, while group-B samples follow equivalent trend and showed slight variation in magnetic and large scattering in physical grain size (Figure 10D).

Discussion

Room, low and high temperature based rock magnetic data, FORC diagrams, XRD and SEM-EDS observations provide vital information about complex magnetic mineral assemblages in the studied cores. Data revealed that the sediment cores from active seep sites have undergone significant diagenetic dissolution in Z-I, while authigenically formed fine-grained magnetite and greigite is predominant in Z-II. Contrastingly, sulfidic (Z-I) and methanic (Z-II) zones of relict core are devoid of authigenic magnetite and mainly dominated by large amount of coarse-grained titanomagnetite and highly coercive (titano hematite) grains of detrital origin which most likely survived the

diagenetic dissolution and remained preserved in these zones (Figures 9I-P). Here, we analyse these information to elucidate the controls of structural and diagenetic (*early versus late*) processes on the sediment magnetic signals in an active/relict cold seep sites in the Bay of Bengal.

Magnetic Mineral Inventory of Sediments at Active/Relict Cold Seep Sites in the K-G Basin

Magnetic mineral assemblages in the sediment cores from active and relict seep sites from K-G basin, primarily consists of detrital (titanomagnetite, titanohematite), diagenetic (greigite/pyrite) and authigenic (magnetite) origin and are present in various proportions (Figures 2, 3, 5, 6, 7, 9I-P). Higher values of χ_{lf} in Z-I can be attributed to the presence of mixture of fine and coarse grained detrital titanomagnetite and titanohematite primarily sourced from Deccan trap basalts (Badesab et al., 2019; Ramesh and Subramanian, 1988; Sangode et al., 2001; Figures 2,7,9I-P). Higher values of grain size indicative (ARM/IRM_{1T}) ratio (Maher, 1988) in Z-II of cores SPC-01/03/04/06, and GC-02 reveals high concentrations of fine SD/PSD magnetite (Figures 2C, O, U, A7, A13). ARM/IRM_{1T} first decreases because of preferential dissolution of fine-grained magnetite in the upper part of the reduced zone (Z-I), and increases later in response to the authigenic formation of fine-grained authigenic magnetite (Lin et al., 2020; Rodelli et al., 2019) and greigite in deeper positions downcore (Z-II). Diagenetically formed magnetic iron sulfide (greigite) are also found to co-exist with detrital titanomagnetite grains and are spatially distributed in both sediment magnetic zones (Z-I and Z-II) of cores from active and relict seep sites (Figures 6, 7, 9I-P, 13). These can be explained based on the fact that few titanomagnetite grains might have survived the early diagenetic dissolution and got rapidly buried and remain preserved due to increased sedimentation.

Verwey transition (T_v) temperatures has been successfully utilized as a diagnostic for discriminating detrital magnetite in sulfidic marine sedimentary systems. For example in Oman continental margin (Chang et al., 2016), offshore of Western Australia (Heslop et al., 2013), and Ria de Vigo, Spain (Mohamed et al., 2011). Low-temperature magnetic data of SPC-01 and SPC-02 revealed the presence of magnetite (Figures 5A, B, D, E, F; Chang et al., 2013, 2014, 2016; Moskowitz et al., 1993; Muxworthy and McClelland, 2000; Özdemir et al., 1993; Prozorov et al., 2007; Verwey et al., 1947). At relict seep site (GC-02), magnetic mineralogy in the high χ_{lf} zone (Z-I) comprised of abundant detrital coarse-grained titanomagnetite and titanohematite particles (Figures 9I-J). Within sulfidic zone, minor peak of high χ_{lf} , $\chi_{fd}\%$, and IRM_{1T}/ χ_{lf} between 11-13 cmbsf reflect the diagenetic formation of greigite in this interval (Figures 2A11, A14, A16, 9K-L). Reduced methane flux due to either closure of underlying fractures/fault or cut-off in the supply of downward diffusing sulfate concentrations most likely interrupted the reductive diagenetic process and rather favoured the formation and preservation of greigite by limiting H₂S production at this site (Jørgensen et al., 2004;

Neretin et al., 2004). Overgrowth of sub-micron sized particles on the larger titanomagnetite grain in Z-II is suggestive of authigenic growth of greigite probably due to weakening of anaerobic oxidation of methane (AOM) process in GC-02 (Figure 9O).

Magnetic granulometry (ARM/IRM_{1T} , IRM_{1T}/χ_{if} ; Maher and Thompson, 1999; Nowaczyk et al., 2012; Roberts, 1995; Sagnotti and Winkler, 1999; Snowball and Thompson, 1990) and mineralogy (S-ratio; Bloemendal et al., 1992) diagnostic parameters exhibits different trends in Z-1 and Z-II, respectively (Figure 2). A trend of down-core decrease of ARM/IRM_{1T} in SPC-01/03/04/05/06 and GC-02 indicates the increase in abundance of coarser magnetic particles in Z-I (Figures 2C, O, U, A1, A7, A13). Loss of finer magnetic fraction in Z-I can be explained by selective diagenetic dissolution of fine-grained magnetic minerals due to their high reactivity and large surface area (Karlin and Levi, 1983; Rodelli et al., 2019; Tarduno, 1995). In contrast, core SPC-02 showed an opposite trend of down-core increase in ARM/IRM_{1T} upto 11 cmbsf in Z-I (Figure 2I). Fining of magnetic particles in Z-I (Figure 2I) can be attributed to diagenetically-induced fining mechanism (Chang et al., 2016) or due to increased production of ultra-fine magnetic grains during magnetite reduction processes (Rodelli et al., 2019; Tarduno, 1995). The titanomagnetite grain in Z-II (Figures 7C, 7L) showed shrinkage-cracks typical of low-temperature maghemitization (Nowaczyk, 2011). The cracks on the grains indicate the areas where dissolution might have started. Hence, the fining mechanism in methanic Z-II can also be linked to the partial dissolution of large titanomagnetite grains (Nowaczyk, 2011). Down-core variations in χ_{if} and IRM_{1T}/χ_{if} illustrate the spatial distribution of magnetic iron sulfides in the studied spade and gravity cores (Figure 2). Apparent linkage between high IRM_{1T}/χ_{if} , $\chi_{fd}\%$, and greigite occurrence was clearly observed for SPC-01/02/04 (Figures 2D, F, L, X, J, V; 6B, C, E, F, J, K; 7B, E, F, J, K, L). Several peaks of IRM_{1T}/χ_{if} and $\chi_{fd}\%$, predominantly in Z-I manifested by presence of non-uniformly distributed greigite (confirmed through SEM-EDS and XRD; Fu et al., 2008; Peters and Dekkers, 2003; Rowan et al., 2009; Figures 2, 6, and 7) can be attributed to non-steady state magnetic mineral diagenesis driven by fluctuations in diffusive methane flux at these sites.

Variability in rock magnetic parameters in each core reflects the different degree of diagenetic disturbances created by methane seepage within the studied sites in the K-G basin. Similar observations were reported from Vestnesa Ridge, Svalbard margin (Szybor and Rasmussen, 2017) and Oregon continental margin (Karlin, 1990). Variations in S-ratio can be attributed to the changes in magnetic mineralogy (Figures 2E, K, Q, W, A3, A9, A15). High S-ratio in Z-I is due to the presence of detrital titanomagnetite (Figures 2E, K, Q, W, A3, A9, A15, 6A, D, G, J, L, 7A, D, G). In spade cores (SPC-01 to SPC-06), we did not observe any signatures of higher coercivity

(hematite) in SEM-EDS and XRD data (Figure 6 and 7). In fact, XRD data confirmed the presence of greigite in samples exhibiting low S-ratio in both Z-I and Z-II (Figures 6B, C, E, F, K). The S-ratio drop in Z-II of relict core can be well-explained by the occurrence of numerous titanohematite grains (Figure 2A15, 9E, O, P). Preservation of titanomagnetite grains (Figures 9M-P) in Z-II could be either due to weakened AOM (Reidinger et al., 2005) or higher resistance against dissolution (Nowaczyk, 2011; Rodelli et al., 2019) which might have hindered the early diagenetic processes and led to the preservation of detrital magnetic particles. Significant drop in S-ratio (Figure 2A15) followed by high $\chi_{fd}\%$ (Figure 2A16) in Z-II of relict core (SSD-45/Stn-11/GC-02) can be attributed to the presence of mixture of detrital titanohematite (Figures 9M, O, P), authigenic greigite (Dillon and Bleil, 2006; Larrasoña et al., 2007; Rodelli et al., 2019) and hexagonal 3C pyrrhotite (Horng, 2018; Horng and Roberts, 2018). Similar observations were recently reported from Perseverance Drift, North-western Weddell Sea (Reilly et al., 2020).

Authigenically formed ferrimagnetic iron sulfides (greigite and pyrrhotite) are well-reported in methane-rich sedimentary system, for instance in Nankai Trough (Horng, 2018; Kars and Kodama, 2015), Hydrate Ridge (Larrasoña et al., 2007), and offshore Taiwan (Horng and Roberts, 2018). FORC diagrams and low-temperature magnetic measurements provided additional constraints on the magnetic mineralogy and domain states. FORC distributions showed the mixture of vortex to multi-domain magnetic particles (Figures 4A–N). In natural system, greigite can commonly occur as magnetostatically interacting framboids. A micromagnetic modelling study involving hysteresis and FORC simulations demonstrated that magnetostatic interactions could remarkably alter the FORC response of greigite framboids and can form patterns similar to vortex and MD (Rodelli et al., 2018; Valdez-Grijalva et al., 2020). It is quite possible that greigite clusters observed in SPC-02 (Figures 7E-F) and SPC-04 (Figure 7J) might be contributing significantly towards the observed FORC (vortex to multi-domain) distributions. Low temperature magnetic data indicated the presence of magnetite in Z-I and Z-II (Figures 5A, B, D, E, F). Similar to our findings, Korff et al. (2016) reported cyclic magnetite dissolution and preservation of detrital magnetite in methanic sediments of the abyssal northwest Pacific Ocean. Sample from the zone of reduced magnetic susceptibility (Z-II) of SPC-01 did not show any indication of a Verwey transition in RT-SIRM, ZFC-FC, and the first derivative of magnetization curves (Figures 5C). We observed that nearly 62 % of the LT-SIRM applied at 5K is lost during warming between 5 and 30 K (Figure 5C). This observation indicates the presence of superparamagnetic (SP) magnetic particles in these samples (Tarduno, 1995; Passier and Dekkers, 2002). Similar to our observation, Kars and Kodama (2015) reported a related pattern of sudden decrease in LT-SIRM from 5 to ~30 K and about ~50–60% loss of the applied remanence in

the sediment core samples from Nankai Trough, offshore Japan. They linked the loss of remanence to the presence of SP particles which get unblocked very rapidly. The SP magnetic particles in this sample (Figure 5C) is most likely iron sulfides like greigite, pyrrhotite, titanohematite (Horng, 2018; Roberts et al., 2020; Rodelli et al., 2019). This interpretation can be explained by the fact that fine-grained magnetic particles in this sample would get readily dissolved in the sulfidic environment (as seen through lowest χ_{fd} in Z-II). Contrastingly, the SP greigite and pyrrhotite nanoparticles are thermodynamically more stable compared to the SP magnetite nanoparticles and would rather remain preserved (Rowan et al., 2009; Roberts et al., 2018; Rodelli et al., 2018). Lack of LT transitions in the magnetization derivation curves in this sample (Figure 5C) is persistent and further confirms the presence of greigite (through high χ_{fd} %, Figure 2F) and pyrrhotite (Chang et al., 2009; Roberts et al., 2011).

Early versus Late Diagenesis of Magnetic Minerals in Active and Relict Methane Seep Sites in the Bay of Bengal: Constraints from Rock Magnetism and Mineralogical proxies

In active cold seep sedimentary system, temporal movement of diagenetic fronts due to variability in methane fluxes and sulfate reduction rates favours non-steady state diagenesis. Such process could generate complex magnetic signatures in sediments involving magnetite reduction and authigenic formation of magnetite (Amiel et al., 2020; Lin et al., 2020; Riedinger et al., 2005) and iron sulfides (Canfield and Berner, 1987; Larrasoana et al., 2003; Liu et al., 2012; Riedinger et al., 2014; Roberts, 2015). Rock magnetic data showed progressive downcore dissolution of magnetite in sediment cores from active (Figures 2A-A10) and relict (Figures 2A11-A16; Karlin and Levi, 1983) sites in K-G basin. A gradual downcore decrease in ARM/IRM_{1T} and χ_{fd} within Z-I in cores SPC-01/03/04/05/06 suggest substantial dissolution of fine-grained magnetic particles due to early diagenesis (Figures 2C, O, U, A1, A7; Rodelli et al., 2019). A slight increase in ARM/IRM_{1T} in Z-II of SPC-01/03/04/06 (Figures 2C, O, U, A7) can be attributed to the presence of fine-grained authigenic magnetite (Karlin et al., 1987; Lin et al., 2020; Roberts, 2015; Roberts et al., 2018; Rodelli et al., 2019). A similar steady increase of ARM/IRM_{1T} in sulfidic zone of a sediment cores from deep methanic zone of Southern Eastern Mediterranean continental shelf (Amiel et al., 2020) and Niger deep-sea fan was attributed to the gradual authigenic growth of SD magnetite (Dillon and Bleil, 2006). A downcore increase in ARM/IRM_{1T} in Z-II of active seep sites (SPC-01/03/04/06) could also be due to presence of authigenic magnetite formed as a result of microbial iron reduction process in methanic sediments which might have permitted the newly formed magnetite to survive the sulfidic dissolution and favoured preservation (Lin et al., 2020; Rodelli et al., 2018, 2019; Figure 2C, O, U, A7). SEM-EDS and XRD data of cores showed the presence of greigite in methanic zone (Z-II) from active seep sites

(Figure 6C, E, F, K, 7E, F, K, L). Following the concept put forward by Lin et al., 2020, we propose that following mechanism for authigenic greigite formation in Z-II of active seep sites. Increased supply of reactive iron (secondary iron oxyhydroxides) produced during iron-sulfide mineral oxidation due to decline in methane seepage intensities (Lin et al., 2016; 2020) and limitation of sulfide in methanic zone (below SMTZ) probably favoured the greigite formation in this zone.

During early diagenesis, sulfate gets readily depleted through decomposition of organic matter (Karlin, 1990a). We put forward the plausible mechanism for the preservation of fine-grained authigenic magnetite in Z-II as seen through a trend of high ARM/IRM_{IT} in SPC-01/03/04/06 (Figure 2C, O, U, A7). Fine-grained magnetite (SD-type) could also occur as magnetic inclusions in silicates which most likely protected the magnetite from diagenetic dissolution (Chang et al., 2016a,b; Feinberg et al., 2005; Hounslow and Morton 2004; Muxworthy and Evans, 2013; Tarduno et al., 2006) and could explain the preservation of fine-grained magnetite in Z-II. Another possibility is that authigenic magnetite formation coupled to microbial iron reduction (Lin et al., 2020) within methanic sediments might have allowed the freshly formed fine-grained magnetite to survive sulfidic dissolution fronts and rather favoured preservation as evident through high ARM/IRM_{IT} values in Z-II (methanic) of cores SPC-01/03/04/06 from active seep sites. However, we do not rule out the possibility of presence of fine-grained titanomagnetite in Z-II. Similar findings were reported from rock magnetic studies on sediment cores from continental margin of Oman north-western Arabian Sea (Chang et al., 2016) and northeast part of Japan Sea (Yamazaki et al., 2003). At relict site, an anomalous (39 – 57 cmbsf) interval within (Z-II) showed increased ARM/IRM_{IT} values and significant drop in S-ratio (29 – 63 cmbsf) indicating the preservation of numerous highly coercive magnetic particles as confirmed through SEM observations (Figures 2A13, A15, 9M-P). We proposed that overgrowth of sub-micron sized authigenically formed SP greigite particles on the larger titanomagnetite grain (at 43 cmbsf, Figure 9O) might have contributed towards the observed increase in IRM_{IT}/ χ_{if} (Figure 2A14). The presence of SP greigite is further confirmed by the observed increase in χ_{fd} % in Z-II of GC-02 (Figure 2A16).

Magnetic iron sulfides including greigite and pyrrhotite forms within the sulfidic pore water produced by upward migrating SMTZ fronts (Kasten et al., 1998; Horng, 2018). Significant downcore decrease in magnetite concentration (χ_{if}) and grain size (ARM/IRM_{IT}) diagnostic parameters in SPC-01/03/04/05/06 and GC-02 suggests that fine-grained magnetic particles were selectively removed by diagenetic dissolution (Figures 2A, C, M, O, S, U, Y, A1, A5, A7, A11, A13; Chang et al., 1987; Karlin et al., 1987; Lin et al., 2020; Roberts, 2015; Rodelli et al., 2019). Rock magnetic (Figure 2), SEM-EDS (Figures 7, 9I-P) observations, and mineralogical (Figures 6, 13)

records provide evidence on the spatial distribution of diagenetically formed iron sulfides (greigite, pyrite) in Z-I and Z-II of all analyzed cores. A noticeable high IRM_{1T}/χ_{lf} and $\chi_{fd}\%$ values in samples from Z-I are exhibited by fine-grained greigite particles formed during early diagenesis (Figure 2). FORC diagrams for majority of samples provided evidences of two important magnetic (fine-grained, SD+SP) populations in Z-I and Z-II (Figures 4A-N). SP sized ultra-fine authigenically formed ferrimagnetic greigite particles (as seen through high $\chi_{fd}\%$ and rapid decrease of ZFC and FC remanences upon warming from 5 to 30K (Banerjee et al., 1993; Muxworthy and Roberts, 2007; Figure 2, 5C) and SD-type (as seen through negative regions in the horizontal axis, Roberts et al., 2011; Rowan and Roberts, 2006; Sagnotti et al., 2005, 2010; Figures 4A-M) indicate the preservation of fine-grained SD magnetite particles.

Reduced magnetization at gas hydrate vents has been established in Cascadia accretionary margin off Vancouver Island (Novosel et al., 2015). At active seep sites, methane is being transported from deep-seated gas reservoir up to the seafloor and the intensities of methane flux governs the SMTZ location. Presence of abundant live chemosynthetic communities (*Bathymodiolus* sp. and *Acharax* sp.) provide evidences of active methane seepage at the studied site (Figures 9A-F). Elevated methane flux will shift the SMTZ fronts upward and vice-versa (Borowski et al., 1996). Production of hydrogen sulfide via AOM at SMTZ causes the dissolution of iron oxides, and precipitation of iron sulfides (Reidinger et al., 2005). Diagenetic dissolution of magnetite followed by the subsequent transformation to pyrite will create a distinct χ_{lf} minima compared to ferrimagnetic greigite which would significantly increase χ_{lf} (Badesab et al., 2019; Dewangan et al., 2013; Kars and Kodama, 2015). Several researchers established that variability in the SMTZ depth can be used to quantify methane flux (Housen and Musgrave, 1996; Larrasoana et al., 2007; Musgrave et al., 2006; Neretin et al., 2004; Novosel et al., 2005; Reidinger et al., 2005; Roberts, 2015). A close linkage between the depth of SMTZ and minima in χ_{lf} has been well-established and increasingly utilized as a proxy for detecting SMTZ fronts in methanic sediments for example in Cascadia margin (Housen and Musgrave, 1996; Larrasoana et al., 2007), offshore of Argentina and Uruguay (Reidinger et al., 2005), Nankai trough, Japan (Kars and Kodama, 2015), and offshore New Zealand (Rowan and Roberts, 2006). In the analyzed sediment cores, the distinct χ_{lf} minima most probably reflect recent SMTZ front, which varies between 5 cmbsf and 16 cmbsf (Figure 2). The shallowest χ_{lf} minima is noticed in active seep core SPC-05 (Figure 2Y) and deepest at SPC-03 (Figure 2M) and relict site GC-02 (Figure 2A11), respectively. Such variability in SMTZ depth provides evidences on the differential rate of diagenesis constrained by fluctuations in methane fluxes. In such non-steady state diagenetic scenario, for instance at active seep sites (SPC-01 to SPC-06), different degree of

diagenetic disturbances created by changing methane flux could variably modify and preserve the primary magnetic mineral assemblages in sediments. SEM observations indicate the presence of abundant coarse-grained titanomagnetite and titanohematite in Z-I (Figures 7A, D, G, 9I-P) and Z-II (Figures 7C, I, 9M-P). More recently Amiel et al. (2020) conducted a detailed magnetic investigation on the sediment cores from SE Mediterranean Continental Shelf to examine the influence of early diagenesis in methanic environment. They reported that rapid sedimentation and non-steady state conditions triggered by variability in methane flux favoured the survival of abundant iron-oxide minerals in the sulfidic and deep methanic zone (Riedinger et al., 2005). In the present study, survival and preservation of these minerals in Z-I and Z-II can be explained by the fact that titanohematite and titanomagnetite are more stable and offers strong resistance to reductive dissolution induced by early and late diagenetic processes (Channell and Hawthorne, 1990; Nowaczyk, 2011; Poulton et al., 2004; Rodelli et al., 2019) or due to increased sedimentation (Amiel et al., 2020, Riedinger et al., 2005). Stability against diagenetic alteration increases together with elevated Ti content and, in turn, results in a higher magnetic stability. Dissolution of titanohematite involves a noticeably slower reaction compared to magnetite (Cornell and Schwertmann, 1996; Liu et al., 2004; Rodelli et al., 2019; Yamazaki et al., 2003). Previous studies have demonstrated that increasing titanium content stabilizes titanomagnetite compounds because Ti^{4+} substitution correspondingly reduces the number of Fe^{3+} , the acting electron acceptor under anaerobic conditions (Karlin, 1990b; Garming et al., 2005). During non-steady diagenesis, formation of secondary minerals takes places whenever pore-water chemistry changes due to upward or downward diffusion of dissolved hydrogen sulfide (Roberts and Weaver, 2005) and could lead to the formation and preservation of authigenic magnetite and greigite. Microbial iron reduction within methanic sediments is the most likely mechanism for authigenic magnetite formation (Lin et al., 2020; Rodelli et al., 2018).

More recently Reilly et al. (2020) and Rodelli et al. (2019) revealed that high coercivity magnetic minerals respond slowly to the diagenetic dissolution through entire SMTZ and can be a potential source for ferric iron via microbial iron reduction process coupled to AOM (Amiel et al., 2020; Beal et al., 2009; Riedinger et al., 2014). They further concluded that increased concentration of high coercivity minerals in methanic zone (below SMTZ) can produce large amount of ferric (Fe^{3+}) via iron reduction where sulfide is limited and favours the authigenic precipitation of greigite. In the relict core (SSD-45/Stn-11/GC-02) greigite and titanohematite are found to occur throughout the sulfidic (Z-I) and methanic (Z-II) (Figure 2A11, A16, 9I-P, 13A-D). It is highly possible that diagenetic dissolution of titanohematites during iron reduction generated enough (Fe^{3+}) and provided

conductive environment for greigite formation in the intervals where sulfide got exhausted in core SSD-45/Stn-11/GC-02. Our SEM (Figures 9K, L, O) and XRD (Figures 13 B,C) observations followed by high values of $\chi_{fd}\%$ (Figure 2A16) support the findings of Reilly et al. (2020). Bivariate magnetic plots (Figure 10) and FORC diagrams (Figure 11) also helped to evaluate the influence of steady and non-steady state diagenetic processes on the magnetic record of sediment cores from active (SPC-01 to SPC-06), relict (Stn-11/GC-02) and paleo (MD161/Stn-8; Mazumdar et al., 2009) seep sites in the K-G basin. Scattered data plot between IRM_{1T}/χ_{lf} and χ_{lf} reflects a broad range of SP greigite (Figure 2A16, 9K, L, O) particles and a larger variations in their concentrations (Figure 10B). A scattered plot between magnetic (ARM/IRM_{1T}) and physical (mean) grain size showed a systematic pattern of fining in magnetic grain size with increase in diagenetic dissolution of detrital magnetic minerals (Figure 10D).

Non-steady state diagenetic processes can potentially affect the sediment magnetic parameters. For example, abrupt change in the sedimentation rate can cause migration of the SMTZ (e.g., Riedinger et al., 2005; Fu et al., 2008), temporal changes in the organic matter load into the sediment can affect the depths of the different respiration processes (Larrasoana et al., 2003; Rowan et al., 2009), changes in the sediment composition can lead to the accumulation of magnetic minerals in the sediment and change in the magnetic parameters. These mechanisms require time-variations in the flux of the sediments from Krishna and Godavari rivers, which are main source of detrital magnetic particles to the studied area. Multiple layers of mass transport deposits (MTD's) generated as a result of frequently occurring high sedimentation events have been identified in the shallow and deep offshore regions of the K-G basin (Ramana et al., 2007; Ramprasad et al., 2011; Yamamoto et al., 2018). Recently Badesab et al., 2019 reported a high resolution sediment magnetic record of high sedimentation events in the K-G basin. Samples from relict site (SSD-45/Stn-11/GC-02) showed remarkably high χ_{lf} and IRM_{1T} (Figures 2A11-A12) compared to active seep sites (SPC-01 to SPC-06) probably due to non-steady state diagenesis driven by high sedimentation events. It is most likely that coarse titanomagnetite and titanohematite grains survived diagenesis due to (1) its inherent property to resist the dissolution (Nowaczyk, 2011; Rodelli et al., 2019), and (2) rapid burial due to increased sedimentation (Badesab et al., 2019). Detailed rock magnetic and microscope analyses conducted on the sediment cores from continental margin of Oman and northern California by Rowan et al. (2009) reported that newly formed greigite particles are small initially and would display thermally unstable SP behaviour unless it grows fully through the stable SD blocking volume. They attributed the magnetic enhancement to the late diagenetic growth of magnetically stable greigite. Greigite can display both SD-type behaviour (Roberts, 1995) as well as

ultrafine-grained SP (Rowan and Roberts, 2006; Rowan et al., 2009). Differences in the growth of greigite particles from active (SPC-01 to SPC-06) and paleo (MD161/Stn-8; Badesab et al., 2020a) samples is clearly reflected in the FORC diagrams (Figures 11A-D). FORC diagram of samples from active seep site (SPC-01) showed the magnetic particles exhibit a mixed (vortex state to multidomain) type behavior (Figure 11A, B; Roberts et al., 2000; Roberts et al., 2017). In contrast, FORC diagrams of paleo-seep samples showed broad distribution with concentric and elongated contour indicative of presence of magnetically stable greigite probably formed as a result of late diagenetic growth (Figure 11C; Rowan et al., 2009) and biogenic mineralization (Figure 11D; Badesab et al., 2020a; Rodelli et al., 2018) at site MD161/Stn-8.

Structural Control on the Formation and Preservation of Greigite

Methane venting episodes linked to active and paleo-cold seeps are well documented in the K-G basin (Dewangan et al., 2020; Mazumdar et al., 2009). High-resolution seismic data across active seep site (SSD-45/Stn-4; present study) showed the presence of well-developed seismic chimney and faults, which facilitated the migration of deep-seated gas through the gas hydrate stability zone (GHSZ) up to the sea floor and favored gas hydrate accumulation in the K-G basin (Dewangan et al., 2020; Figure 1B). At the same site, shallow (2-3 mbsf) gas hydrates were recovered during a gas hydrate exploration cruise in 2018 (Mazumdar et al., 2019). Vertical migration of methane through the sedimentary column produces multiple AOM's resulting in the growth of diagenetic minerals including pyrite, greigite and pyrrhotite (Roberts, 2015). Interplay between the rates downward diffusing sulfate and upward migrating methane concentrations control the amount of hydrogen sulfide which is a key factor constraining the greigite formation (Jørgensen et al., 2004; Kasten et al., 1998; Neretin et al., 2004). For instance, enhanced methane flux would generate large amount of hydrogen sulfide which could drive pyritization process to complete resulting in the precipitation of pyrite, while limitation of sulfide due to decline in methane would favor greigite/pyrrhotite formation (Liu et al., 2004).

At active site, presence of greigite in both sediment magnetic zones of cores SPC-01/02/04 has been confirmed through SEM-EDS and XRD data (Figures 2, 6, 7). We try to investigate the structural control on the variability in methane fluxes and subsequent diagenetic formation of greigite in the studied cores. Control of opening and closing dynamics of the underlying fracture/fault system on methane migration in the K-G basin has been well-established (Dewangan et al., 2011; 2020;). Spatial distribution of authigenic carbonates in cores SPC-01, SPC-04, SPC-06 (Figure 14) provide evidence on several AOM's and is indicative of past fluctuations in methane fluxes. We put forward following plausible mechanisms to explain the formation and preservation of greigite in Z-I and Z-II:

(1) decline in methane flux either due to massive hydrate accumulation (Dewangan et al., 2020; Mazumdar et al., 2019) or hindering of upward migrating fluid/gas by the carbonate layers in the subsurface sediments most likely resulted in low sulfide production and preferentially favoured formation and preservation of greigite in the Z-I. Similar observations were reported in fault-controlled cold seep-hydrate Woolsey Mound in the Northern Gulf of Mexico (Simonetti et al., 2013), gas hydrate field offshore Vancouver Island (Riedel et al., 2002), Vestnesa Ridge, W-Svalbard Margin (Singhroha et al., 2020), and in the K-G basin (Badesab et al., 2017; Dewangan et al., 2011). They explained that plugging of an active fault system due to massive hydrate formation can also cause significant drop in methane flux. (2) Occurrence of greigite below the carbonate layers in cores SPC-01, SPC-04, SPC-06 (Figure 14) in Z-II suggest that supply of downward diffusing sulfide is most likely hindered and subsequently a sulfide deficient zone is formed below the carbonate layer which inhibited the pyritization and rather favoured the formation and preservation of greigite. A detailed rock magnetic analysis of a 30 m long sediment core from paleo-seep site in the Bay of Bengal reported the presence of both diagenetic and biogenic greigite (within 17-23 mbsf) i.e., beneath a thick layer of authigenic carbonate formed as a result of intense methane seepage event (Badesab et al., 2020a; Dewangan et al., 2013; Mazumdar et al., 2009). More recent study has demonstrated that elevated supply of Fe^{2+} via iron reduction produced by high coercivity minerals in sulfide limited zone (Z-II) can also favour the authigenic growth of greigite (Reilly et al., 2020; Rodelli et al., 2019). Greigite presence in low S-ratio intervals of Z-II in relict core (SSD-45/Stn-11/GC-02) can also be linked with such process (Figure 2A15, 9O, 13C-D). The presence of greigite is further confirmed by the observed increase in $\chi_{fd}\%$ (Figure 2A16). However additional geochemical and microbiological data are warranted to resolve the mechanism.

A conceptual model explaining the evolution of magnetic mineralogies at active (Stn-4/SPC-01 to SPC-06) and relict (Stn-11/GC-02) seep sites is developed (Figure 12). Shallow gas hydrates (2-3 mbsf) and authigenic carbonates (throughout the cores) were recovered at active seep sites (Figure 14; Mazumdar et al., 2019). In sulfidic (Z-I), detrital magnetic particles minerals supplied through Krishna and Godavari river systems reacted with the H_2S produced by bacterial activity via organic matter decomposition and AOM-coupled sulfate reduction which led to the diagenetic dissolution of magnetic particles and subsequent precipitation of iron sulfide (pyrite) with intermediate precursors such as greigite and pyrrhotite (Berner, 1984; Karlin, 1990a). SEM-EDS and XRD data coupled with $\chi_{fd}\%$ confirmed the presence of greigite in both sulfidic (Z-I) and methanic (Z-II) (Figure 2, 6, 7). Most likely mechanism which can explain the formation and preservation of greigite in Z-I and Z-II is as follows. Decline in methane flux due to massive hydrate accumulation along the active fault

system and formation of authigenic carbonate crust in the sub-surface sediments might have hindered the supply of upward migrating fluid/gas and limited the sulfide production which preferentially enhanced greigite formation in Z-I. Secondly, restricted supply of downward diffusing sulfide by the carbonate layers in the uppermost sediments might be a responsible process for creating a sulfide deficient zone beneath. These might have inhibited the pyritization process and rather favoured the formation of greigite in methanic zone (Z-II). Samples from relict site (SSD-45/Stn-11/GC-02) showed notably high χ_{lf} and IRM_{IT} (Figures 2 A11-A12) compared to active seep sites which is most probably due to non-steady state diagenesis driven by high sedimentation events in the K-G basin. Coarse titanomagnetite and titanohematite grains might have survived diagenesis either due to its inherent property to resist the dissolution (Nowaczyk, 2011; Rodelli et al., 2019), or because of rapid burial due to increased sedimentation (Badesab et al., 2019).

Conclusions

A set of rock magnetic, mineralogical and sedimentological records of the sediment cores were used to characterize the changes in the magnetic concentration, grain size, and mineralogy in a newly discovered active (Stn-4/SPC-01 to SPC-06) and relict (Stn-11/GC-02) cold seep sites in the K-G basin, Bay of Bengal. Sediment magnetism is mainly carried by complex magnetic mineral assemblages of detrital (titanomagnetite, titanohematite) and authigenic (magnetite, greigite) minerals. Topmost sulfidic sediment magnetic zone (Z-I) is marked by a higher concentration of magnetic minerals as evident in rock magnetic parameters. A systematic downcore decrease in χ_{lf} and IRM_{IT} in this zone is due to the progressive diagenetic dissolution of iron oxide and subsequent precipitation of iron sulfides. Magnetogranulometric proxy (ARM/IRM_{IT}) provided valuable insights on the preferential dissolution of fine-grained magnetite in the sulfidic zone (Z-I), and authigenic formation of magnetite in methanic zone (Z-II) of all studied cores. At relict site, elevated concentration of highly coercive magnetic (titanohematite) grains relative to soft minerals (as seen through lower S-ratio and χ_{lf}) which survived diagenesis are found in the methanic zone. A strong linkage between occurrence of authigenic carbonates and greigite formation and preservation is noticed. We summarized our observations into a conceptual model which provides insights on the evolution of different magnetic mineralogies constrained by variable diagenetic processes at active and relict seep sites in the K-G basin, Bay of Bengal.

Data Availability Statement

The data used in the present study are available on CSIR-NIO's data repository (<https://publication-data.nio.org/s/pb7ZQHybKm5DqDj>).

Author Contributions

VG, FB, PD and MK developed the concept for the manuscript. PD and VG have contributed towards sediment core collection and sampling during the research expedition (SSD-045) onboard R/V Sindhu Sadhana. Analyses were performed by VG, FB and PD. All authors contributed equally to the writing and editing of the manuscript and preparation of figures and table.

Acknowledgments

Director, CSIR–NIO, Secretary MOES, and National Gas Hydrate Program (NGHP) are thanked for supporting this study. We greatly acknowledge the support of Dr. Aninda Mazumdar, participants of scientific cruise SSD-045 onboard research vessel R/V Sindhu Sadhana of CSIR-NIO, ship cell team and crews onboard for providing assistance in collection of sediment cores and sampling. Director of the Center for Advanced Marine Core Research (CMCR), Kochi University, Japan is thanked for allowing access to the Paleomagnetic laboratory during a research visit of Firoz Badesab as a part of INSA-JSPS fellowship. Myriam Kars is thanked for providing support to Dr. Firoz Badesab during the fellowship period at CMCR. High-end rock magnetic analyses at CMCR were supported by DST-JSPS under the scheme JSPS Postdoctoral Fellowship for Overseas Researchers (Strategic Program; JSPS grant GR 17202) and Establishment of Young Researcher Fellowship Programme 2017–2018 (IA/ Indo-Japanese/F-1/2018) scheme awarded to F. B. We thank Chisa Nishimori for providing laboratory and technical support in Kochi. Thanks to Areef Sardar, Girish Prabhu, Kaveri Salunke and Prem Piyush Panda for their support in carrying out mineralogical analyses at CSIR-NIO. We thank associate editor (Luigi Jovane) and all three reviewers for constructive comments that improved the paper. The authors declare no conflicts of interests. The data used in the present study are available on CSIR-NIO's data repository (<https://publication-data.nio.org/s/pb7ZQHybKm5DqDj>). This is CSIR-NIO publication no. XXX.

Figure Caption

Figure 1. (A) Map showing the location of active (SSD-45/Stn-4), relict (SSD-45/Stn-11/GC-02) and paleo (MD161/Stn-08) seep sites in the Krishna-Godavari (K-G) basin, Bay of Bengal High resolution seismic profile (P1) highlighting (b) the normal faults (blue dashed lines), subsurface chimney like feature (solid red lines) and water column imaging showing gas flares (orange). Regional toe-thrust fault (yellow dashed line), feasible BSR (white dashed line), and subsurface horizons (solid black lines) are marked on the seismic section (modified after Dewangan et al., 2020). The spade sediment cores SPC-01, SPC-02, SPC-03, SPC-04, SPC-05, and SPC-06 were retrieved from active seep site SSD-45/Stn-4 and gravity core GC-02 was retrieved from relict site SSD-45/Stn-11. The location of the sediment core from paleo-seep site (MD161/Stn-8) is also marked. Bathymetry data of the studied area was obtained from GEBCO Compilation Group665 (2020) GEBCO 2020 Grid (doi: 10.5285/a29c5465-b138-234d-e053-6c86abc040b9).

Figure 2. Down-core variations of selected rock magnetic data of spade (A-E): SPC-01, (F-J): SPC-02, (K-O): SPC-03, (P-T): SPC-04, (U-Y): SPC-05, (Z-A4): SPC-06, and gravity sediment cores (A5-A9): GC-02. Based on magnetic susceptibility variations two sedimentary magnetic zones Z-I and Z-II are demarcated. Z-I highlighted with gray shading. (Please note that χ_{lf} = low frequency magnetic susceptibility, ARM = anhysteretic remanent magnetization, and IRM_{1T} = isothermal remanent magnetization, χ_{fd} % = frequency dependent susceptibility). Depth of carbonate occurrence are highlighted in solid black arrows (horizontal). The depth of greigite occurrence is marked by “G”. Sediment magnetic zones (Z-I, Z-II) in each profile are marked.

Figure 3. Thermomagnetic profiles of selected representative samples representing two sedimentary magnetic zones of the studied spade sediment cores. (A-B): SPC-01, (C-D): SPC-02, (E-F): SPC-03, and (G-H): SPC-05. Solid red lines indicate heating curves, and blue lines indicate cooling curves respectively.

Figure 4. First-order reversal curve diagrams for selected representative samples from spade cores. (A-D): SPC-01, (E-H): SPC-02, (I-J): SPC-03, (K-L): SPC-05, and (M-N): SPC-06.

Figure 5. Low-temperature magnetization curves for selected representative samples from the two spade cores (A-C): SPC-01 and (D-F): SPC-02. FC = field-cooled, RTSIRM = saturation isothermal remanent magnetization at room temperature, ZFC = zero field-cooled. The corresponding values of Verwey transition (T_v) are placed near the first derivative of magnetization curves.

Figure 6. X-ray diffraction spectra for magnetic minerals extracted from different sediment core depth intervals of spade cores. (A-C): SPC-01, (D-F): SPC-02, (G-I): SPC-03, (J-K): SPC-04, and (L-M): SPC-05. TM = titanomagnetite, P = pyrite, Qz = quartz, and G = greigite.

Figure 7. Scanning electron microscopy on magnetic extracts from different sediment core depth intervals. Energy dispersive x-ray spectroscopy spectra are placed adjacent to the respective images. (A-C): SPC-01, (D-F): SPC-02, (G-I): SPC-03, and (J-L): SPC-04. Iron (Fe), titanium (Ti), sulfur (S), oxygen (O), calcium (Ca), silicon (Si), carbon (C), aluminium (Al), potassium (K), magnesium (Mg), and manganese (Mn) peaks are indicated.

Figure 8. Grain size distribution and magnetic susceptibility data of all spade (SPC-01 to SPC-06) sediment cores retrieved from active methane seep site SSD-45/Stn-4. Depths of carbonate occurrence are highlighted in solid red arrows (vertical). The depth of greigite occurrence is marked by “G”. Sediment magnetic zones (Z-I, Z-II) in each profile are marked.

Figure 9. Photographs showing occurrence of (A, B, C, E): *Bathymodiolus* sp., (D): Decapod crustaceans (squat lobsters), (F): *Acharax* sp. found at the spade core (surface) locations, (G) *calyptogena* sp., shell fragment, and (H) authigenic carbonates found at 48 cmbsf in GC-02 location. (I–P): Scanning electron microscopy on magnetic extracts from different sediment core depth intervals (Relict seep site: SSD-45/Stn-11/GC-02). TM = titanomagnetite, TH = titanohematite, and G = greigite).

Figure 10. (A–D): Bivariate scatter plots of magnetic parameters magnetic susceptibility (χ_{lf}), saturation isothermal remanent magnetization (IRM_{1T}), IRM_{1T}/χ , S-ratio, ARM/ IRM_{1T} and mean grain size for spade cores (SPC-01 to SPC-06) from active (SSD-45/Stn-4) and gravity core (GC-02) from relict seep site (SSD-45/Stn-11) in the Krishna-Godavari (K-G) basin, Bay of Bengal. The gray arrows are used to highlight the trends in plots.

Figure 11. Comparative FORC diagrams of greigite bearing sediment intervals from (A-B): active (SSD-45/Stn-4/SPC-01) and (C-D) of paleo-seep location (MD161-Station-08; modified from Badesab et al., 2020a) in the Krishna-Godavari (K-G) basin, Bay of Bengal. The dashed (black) lines along Bc axis highlights the negative region on the horizontal axis.

Figure 12. Conceptual model explaining the structural and diagenetic controls on the evolution of magnetic mineralogies at active and relict methane seep site in the Krishna-Godavari (K-G) basin, Bay of Bengal.

Figure 13. (A-D) X-ray diffraction spectra for magnetic minerals extracted from different sediment intervals of relict seep site: SSD-45/ Stn-11/GC-02. TM = titanomagnetite, H = hematite, Py= pyrite, and G = greigite

Figure 14. Photographs showing methane-derived authigenic carbonates found in an active seep sites SSD-45/Stn-04/SPC-01, SPC-04 and SPC-06. Respective depths of the carbonate occurrence are mentioned.

Table 1. Information of spade sediment cores retrieved from an active seep site in the Krishna-Godavari (K-G) basin, Bay of Bengal.

References

- Amiel, N., Shaar, R., and Sivan, O. (2020). The Effect of Early Diagenesis in Methanic Sediments on Sedimentary Magnetic Properties: Case Study From the SE Mediterranean Continental Shelf. *Frontiers in Earth Science*, 8:283. doi:10.3389/feart.2020.00283
- Badesab, F., Dewangan, P., Gaikwad, V., Kars, M., Kocherla, M., Krishna, K.S., et al. (2019). Magnetic mineralogical approach for exploration of gas hydrates in the Bay of Bengal. *Journal of Geophysical Research: Solid Earth*, 24(5), 4428–4451. doi:10.1029/2019JB017466
- Badesab, F., Gaikwad, V., and Dewangan, P. (2020a). Controls on greigite preservation in a gas hydrate system of the Krishna-Godavari basin, Bay of Bengal. *Geo-Mar. Lett.*, 40(4), 439-452. doi:10.1007/s00367-019-00604-z
- Badesab, F., Dewangan, P., Gaikwad, V., Sebastian, J. G., and Venkateshwarlu, M. (2020b). A rock magnetic perspective of gas hydrate occurrences in a high-energy depositional system in the Krishna-Godavari basin, Bay of Bengal. *Geo-Mar. Lett.*, 1-15. doi:10.1007/s00367-020-00646-8
- Badesab, F., Dewangan, P., and Gaikwad, V. (2020c). Magnetic mineral diagenesis in a newly discovered active cold seep site in the Bay of Bengal. *Front. Earth Sci.* doi:10.3389/feart.2020.592557
- Badesab, F., Dewangan, P., Usapkar, A., Kocherla, M., Peketi, A., Mohite, K., et al. (2017). Controls on evolution of gas-hydrate system in the Krishna-Godavari basin, offshore India. *Geochem., Geophys., Geosys*, 18(1), 52–74. doi:10.1002/2016GC006606
- Banerjee, S. K., Hunt, C. P., and Liu, X. M. (1993). Separation of local signals from the regional paleomonsoon record of the Chinese Loess Plateau: A rock-magnetic approach. *Geophys. Res. Lett.*, 20(9), 843-846. doi:10.1029/93GL00908
- Bastia, R. (2007). Geologic settings and petroleum systems of India's east coast offshore basins: Concepts and applications. Bangalore, India: *Technology Publications*.
- Beal, E. J., House, C. H., and Orphan, V. J. (2009). Manganese-and iron-dependent marine methane oxidation. *Science*, 325(5937), 184-187. doi:10.1126/science.1169984
- Berndt, C., Feseker, T., Treude, T., Krastel, S., Liebetrau, V., Niemann, H., et al. (2014). Temporal constraints on hydrate-controlled methane seepage off Svalbard. *Science*, 343(6168), 284–287. doi:10.1126/science.1246298
- Besnus, M. J., and Meyer, A. J. (1964). Nouvelles données expérimentales sur le magnétisme de la pyrrhotine naturelle. *In Proc. Int. Conf. Mag* (Vol. 20, pp. 507-511).
- Biksham, G., and Subramanian, V. (1988). Sediment transport of the Godavari River basin and its controlling factors. *J. Hydrol.*, 101(1-4), 275-290. doi:10.1016/0022-1694(88)90040-6
- Bloemendal, J., King, J.W., Hall, F.R., and Doh, S.J. (1992) Rock magnetism of late Neogene and Pleistocene deep-sea sediments: relationship to sediment source, diagenetic processes, and sediment lithology. *J. Geophys. Res. Solid Earth*, 96:4361–4375. doi:10.1029/91JB03068

- Boetius, A., Ravensschlag, K., Schubert, C.J., Rickert, D., Widdel, F., Gieseke, A., et al. (2000) A marine microbial consortium apparently mediating anaerobic oxidation of methane: *Nature*, v. 407, p. 623–626, doi:10.1038/35036572.
- Bohrmann, G., Ivanov, M., Foucher, J. P., Spiess, V., Bialas, J., Greinert, J., et al. (2003). Mud volcanoes and gas hydrates in the Black Sea: new data from Dvurechenskii and Odessa mud volcanoes. *Geo-Mar. Lett.*, 23(3-4), 239-249. doi:10.1007/s00367-003-0157-7
- Borowski, W. S., Paull, C. K., and Ussler, W. III. (1996). Marine pore-water sulfate profiles indicate in situ methane flux from underlying gas hydrate. *Geology*, 24(7), 655–658. doi:10.1130/0091-7613(1996)024<0655:MPWSPI>2.3.CO;2
- Bünz, S., Polyanov, S., Vadakkepuliambatta, S., Consolaro, C., and Mienert, J. (2012). Active gas venting through hydrate-bearing sediments on the Vestnesa Ridge, offshore W-Svalbard. *Mar. Geol.*, 332–334, 189–197. doi:10.1016/j.margeo.2012.09.012
- Canfield, D. E., and Berner, R. A. (1987). Dissolution and pyritization of magnetite in anoxic marine sediments. *Geochim. Cosmochim. Acta*, 51(3), 645–659. doi:10.1016/0016-7037(87)90076-7
- Chang, L., Roberts, A. P., Rowan, C. J., Tang, Y., Pruner, P., Chen, Q., et al. (2009) Low-temperature magnetic properties of greigite (Fe₃S₄). *Geochem., Geophys. Geosy.*, 10, Q01Y04. doi:10.1029/2008GC002276
- Chang, L., Heslop, D., Roberts, A.P., Rey, D., and Mohamed, K.J. (2016b). Discrimination of biogenic and detrital magnetite through a double Verwey transition temperature. *J. Geophys. Res. Solid Earth*, 121(1):3–14. doi:10.1002/2015JB012485
- Chang, L., Roberts, A.P., Heslop, D., Hayashida, A., Li, J., Zhao, X. et al. (2016a). Widespread occurrence of silicate-hosted magnetic mineral inclusions in marine sediments and their contribution to paleomagnetic recording. *J. Geophys. Res. Solid Earth*, 121(12):8415–8431. doi:10.1002/2016JB013109
- Chang, L., Roberts, A.P., Winklhofer, M., Heslop, D., Dekkers, M.J., Krijgsman, W., et al. (2014). Magnetic detection and characterization of biogenic magnetic minerals: a comparison of ferromagnetic resonance and first-order reversal curve diagrams. *J. Geophys. Res. Solid Earth*, 119(8):6136–6158. doi:10.1002/2014JB011213
- Chang, L., Winklhofer, M., Roberts, A. P., Heslop, D., Florindo, F., Dekkers, M. J., et al. (2013). Low-temperature magnetic properties of pelagic carbonates: Oxidation of biogenic magnetite and identification of magnetosome chains. *J. Geophys. Res. Solid Earth*, 118(12), 6049–6065. doi:10.1002/2013JB010381
- Chang, S. B. R., Kirschvink, J. L., and Stolz, J. F. (1987). Biogenic magnetite as a primary remanence carrier in limestone deposits. *Phys. Earth Planet. Inter.* 46, 289–303. doi:10.1016/0031-9201(87)90191-9
- Channell, J. E. T., and Hawthorne, T. (1990). Progressive dissolution of titanomagnetites at ODP Site 653 (Tyrrhenian Sea). *Earth Planet. Sci. Lett.*, 96(3-4), 469–480. doi:10.1016/0012-821X(90)90021-O

Collett, T., Riedel, M., Cochran, J. R., Boswell, R., Presley, J., Kumar, P., et al., and the NGHP Expedition 01 Scientists (2008). Indian National Gas Hydrate Program, Expedition - 01, Initial report, Directorate General of Hydrocarbons, Ministry of Petroleum and Natural gas, India.

Cornell, R. M., and Schwertmann, U. (1996). *The Iron Oxides*, VCH.

Crémière, A., Chanda, S., Sahy, D., Thorsnes, T., Martmad, T., Noblec, S.R. et al. (2018). Structural controls on seepage of thermogenic and microbial methane since the last glacial maximum in the Harstad Basin, southwest Barents Sea. *Mar. Petrol. Geol.*, 98 (2018) 569–58. doi:10.1016/j.marpetgeo.2018.07.010

Dekkers, M. J. (1989). Magnetic properties of natural pyrrhotite. II. High- and low-temperature behaviour of Jrs and TRM as function of grain size. *Phys. Earth Planet. Inter.*, 57, 266–283. doi:10.1016/0031-9201(89)90116-7

Dewangan, P., Basavaiah, N., Badesab, F. K., Usapkar, A., Mazumdar, A., Joshi, R., et al. (2013). Diagenesis of magnetic minerals in a gas hydrate/cold seep environment off the Krishna–Godavari basin, Bay of Bengal. *Mar. Geol.*, 340, 57–70. doi:10.1016/j.margeo.2013.04.016

Dewangan, P., Ramprasad, T., Ramana, M. V., Mazumdar, A., Desa, M., and Badesab, F. K. (2010). Seabed morphology and gas venting features in the continental slope region of Krishna–Godavari basin, Bay of Bengal: Implications in gas-hydrate exploration. *Mar. Petrol. Geol.*, 27(7), 1628–1641. doi:10.1016/j.marpetgeo.2010.03.015

Dewangan, P., Sriram, G., Kumar, A., Mazumdar, A., Peketi, A., Mahale, V. et al. (2020). Widespread occurrence of methane seeps in deep-water regions of Krishna–Godavari basin, Bay of Bengal. *Mar. Petrol. Geol.*, 104783. doi:10.1016/j.marpetgeo.2020.104783

Dewangan, P., Sriram, G., Ramprasad, T., Ramana, M. V., and Jaiswal, P. (2011). Fault system and thermal regime in the vicinity of site NGHP-01-10, Krishna–Godavari basin, Bay of Bengal. *Mar. Petrol. Geol.*, 28, 1899–1914. doi:10.1016/j.marpetgeo.2011.03.009

Dillon, M., and Bleil, U. (2006). Rock magnetic signatures in diagenetically altered sediments from the Niger deep-sea fan. *J. Geophys. Res. Solid Earth*, 111(B3). doi:10.1029/2004JB003540

Feinberg, J. M., Scott, G. R., Renne, P. R., and Wenk, H. R. (2005). Exsolved magnetite inclusions in silicates: Features determining their remanence behavior. *Geology*, 33(6), 513–516. doi:10.1130/G21290.1

Florindo, F., Karner, D. B., Marra, F., Renne, P. R., Roberts, A. P., and Weaver, R. (2007). Radioisotopic age constraints for Glacial Terminations IX and VII from aggradational sections of the Tiber River delta in Rome, Italy. *Earth Planet. Sci. Lett.*, 256(1-2), 61–80. doi:10.1016/j.epsl.2007.01.014

Frank, U., and Nowaczyk, N. R. (2008). Mineral magnetic properties of artificial samples systematically mixed from haematite and magnetite. *Geophys. J. Inter.*, 175(2), 449–461. doi:10.1111/j.1365-246X.2008.03821.x

Fu, Y., Von Dobeneck, T., Franke, C., Heslop, D., and Kasten, S. (2008). Rock magnetic identification and geochemical process models of greigite formation in Quaternary marine sediments from the Gulf of Mexico (IODP Hole U1319A). *Earth Planet. Sci. Lett.*, 275(3-4), 233–245. doi:10.1016/j.epsl.2008.07.034

- Garming, J. F. L., Bleil, U., and Riedinger, N. (2005). Alteration of magnetic mineralogy at the sulfate–methane transition: Analysis of sediments from the Argentine continental slope. *Phys. Earth Planet. Inter.*, 151(3-4), 290–308. doi:10.1016/j.pepi.2005.04.001
- Geersen, J., Scholz, F., Linke, P., Schmidt, M., Lange, D., Behrmann, J.H., et al. (2016). Fault zone controlled seafloor methane seepage in the rupture area of the 2010 Maule earthquake, Central Chile. *Geochem., Geophys., Geosys.* 17(11), pp.4802-4813. doi:10.1002/2016GC006498
- Gullapalli, S., Dewangan, P., Kumar, A., Dakara, G., and Mishra, C. K. (2019). Seismic evidence of free gas migration through the gas hydrate stability zone (GHSZ) and active methane seep in Krishna-Godavari offshore basin. *Mar. Petrol. Geol.*, 110, 695-705. doi:10.1016/j.marpetgeo.2019.07.052
- Harrison, R. J., and Feinberg, J. M. (2008). FORCinel: An improved algorithm for calculating first order reversal curve distributions using locally weighted regression smoothing. *Geochem., Geophys., Geosys.* 9, Q05016. doi:10.1029/2008GC001987
- Henry, P., Lallemand, S., Nakamura, K. I., Tsunogai, U., Mazzotti, S., and Kobayashi, K. (2002). Surface expression of fluid venting at the toe of the Nankai wedge and implications for flow paths. *Mar. Geol.*, 187(1-2), 119-143. doi:10.1016/S0025-3227(02)00262-1
- Heslop, D., Roberts, A. P., Chang, L., Davies, M., Abrajevitch, A., and Deckker, P. (2013). Quantifying magnetite magnetofossil contributions to sedimentary magnetizations. *Earth Planet. Sci. Lett.*, 382, 58-65. doi:10.1016/j.epsl.2013.09.011
- Hirt, A. M., and Gehring, A. U. (1991). Thermal alteration of the magnetic mineralogy in ferruginous rocks. *J. Geophys. Res. Solid Earth*, 96(B6), 9947–9953. doi:10.1029/91JB00573
- Horng, C. S. (2018). Unusual magnetic properties of sedimentary pyrrhotite in methane seepage sediments: Comparison with metamorphic pyrrhotite and sedimentary greigite. *J. Geophys. Res. Solid Earth*, 123(6), 4601-4617. doi:10.1002/2017JB015262
- Horng, C. S., and Chen, K. H. (2006). Complicated magnetic mineral assemblages in marine sediments offshore southwestern Taiwan: Possible influences of methane flux on the early diagenetic process. *Terr., Atmos. Ocean. Sci.*, 17, 1009–1026. doi:10.3319/TAO.2006.17.4.1009(GH)
- Horng, C. S., and Roberts, A. P. (2018). The low-temperature Besnus magnetic transition: Signals due to monoclinic and hexagonal pyrrhotite. *Geochem., Geophys., Geosys.*, 19, 3364–3375. doi:10.1029/2017GC007394
- Hounsflow, M. W., & Morton, A. C. (2004). Evaluation of sediment provenance using magnetic mineral inclusions in clastic silicates: comparison with heavy mineral analysis. *Sedimentary Geology*, 171(1-4), 13-36. doi:10.1016/j.sedgeo.2004.05.008
- Housen, B. A., & Musgrave, R. J. (1996). Rock-magnetic signature of gas hydrates in accretionary prism sediments. *Earth Planet. Sci. Lett.*, 139(3-4), 509–519. doi:10.1016/0012-821X(95)00245-8
- Jørgensen, B. B., Böttcher, M. E., Lüschen, H., Neretin, L. N., and Volkov, I. I. (2004). Anaerobic methane oxidation and a deep H₂S sink generate isotopically heavy sulfides in Black Sea sediments. *Geochim. Cosmochim. Acta*, 68(9), 2095–2118. doi:10.1016/j.gca.2003.07.017

- Karlin, R. (1990). Magnetic mineral diagenesis in suboxic sediments at Bettis site W-N, NE Pacific Ocean. *J. Geophys. Res. Solid Earth*, 95(B4), 4421-4436. doi:10.1029/JB095iB04p04421
- Karlin, R. (1990a). Magnetite diagenesis in marine sediments from the Oregon continental margin. *J. Geophys. Res. Solid Earth*, 95(B4), 4405-4419. doi:10.1029/JB095iB04p04405
- Karlin, R., and Levi, S. (1983). Diagenesis of magnetic minerals in recent haemipelagic sediments. *Nature*, 303(5915), 327. doi:10.1038/303327a0
- Karlin, R., Lyle, M., and Heath, G. R. (1987). Authigenic magnetite formation in suboxic marine sediments. *Nature*, 326(6112), 490-493.
- Kars, M., and Kodama, K. (2015). Authigenesis of magnetic minerals in gas hydrate bearing sediments in the Nankai Trough, Offshore Japan. *Geochem., Geophys., Geosys*, 16, 947–961. doi:10.1002/2014GC005614
- Kasten, S., Freudenthal, T., Gingele, F. X., and Schulz, H. D. (1998). Simultaneous formation of iron-rich layers at different redox boundaries in sediments of the Amazon deep-sea fan. *Geochim. Cosmochim. Acta*, 62, 2253–2264. doi:10.1016/S0016-7037(98)00093-3
- Knittel, K., and Boetius, A. (2009). Anaerobic oxidation of methane: Progress with an unknown process. *Ann. Rev. Microb.*, 63,311–334. doi:10.1038/296643a0
- Kopp, R. E., and Kirschvink, J. L. (2008). The identification and biogeochemical interpretation of fossil magnetotactic bacteria. *Earth-Sci. Rev.*, 86(1-4), 42-61. doi:10.1016/j.earscirev.2007.08.001
- Korff, L., von Dobeneck, T., Frederichs, T., Kasten, S., Kuhn, G., Gersonde, R., and Diekmann, B. (2016). Cyclic magnetite dissolution in Pleistocene sediments of the abyssal northwest Pacific Ocean: evidence for glacial oxygen depletion and carbon trapping. *Paleoceanography*, 31(5), 600-624. doi:10.1002/2015PA002882
- Kumar, P., Collett, T. S., Boswell, R., Cochran, J. R., Lall, M., Mazumdar, A., et al. (2014). Geologic implications of gas hydrates in the offshore of India: Krishna-Godavari Basin, Mahanadi Basin, Andaman Sea, Kerala–Konkan Basin. *Mar. Petrol. Geol.*, 58,29–98. doi:10.1016/j.marpetgeo.2014.07.031
- Larrasoña, J. C., Roberts, A. P., Musgrave, R. J., Gràcia, E., Piñero, E., Vega, M., et al. (2007). Diagenetic formation of greigite and pyrrhotite in gas hydrate marine sedimentary systems. *Earth Planet. Sci. Lett.*, 261(3-4), 350–366. doi:10.1016/j.epsl.2007.06.032
- Larrasoña, J. C., Roberts, A. P., Stoner, J. S., Richter, C., and Wehausen, R. (2003). A new proxy for bottom-water ventilation in the eastern Mediterranean based on diagenetically controlled magnetic properties of sapropel-bearing sediments. *Palaeogeogr., Palaeoclimatol., Palaeoecol.*, 190, 221-242. doi:10.1016/S0031-0182(02)00607-7
- Lascu, I., Einsle, J. F., Ball, M. R., and Harrison, R. J. (2018). The vortex state in geologic materials: A micromagnetic perspective. *J. Geophys. Res. Solid Earth*, 123, 7285–7304. doi:10.1029/2018JB015909
- Lattard, D., Engelmann, R., Kontny, A., & Sauerzapf, U. (2006). Curie temperatures of synthetic titanomagnetites in the Fe-Ti-O system: Effects of composition, crystal chemistry, and thermomagnetic methods. *J. Geophys. Res. Solid Earth*, 111(B12).

- Lin, Z., Sun, X., Strauss, H., Lu, Y., Böttcher, M.E., Teichert, B.M., et al. (2018). Multiple sulfur isotopic evidence for the origin of elemental sulfur in an iron-dominated gas hydrate-bearing sedimentary environment. *Mar. Geol.*, 403, pp.271-284. doi:10.1016/j.margeo.2018.06.010.
- Lin, Z., Sun, X., Lu, Y., Strauss, H., Xu, L., Gong, J., et al. (2017). The enrichment of heavy iron isotopes in authigenic pyrite as a possible indicator of sulfate-driven anaerobic oxidation of methane: Insights from the South China Sea. *Chem. Geol.*, 449, pp.15-29. doi:10.1016/j.chemgeo.2016.11.032
- Lin, Z., Sun, X., Roberts, A.P., Strauss, H., Lu, Y., Yang, X., et al. (2020). A novel authigenic magnetite source for sedimentary magnetization. *Geology*. doi:10.1130/G48069.1
- Lin, Q., Wang, J., Algeo, T.J., Su, P., Hu, G. (2016). Formation mechanism of authigenic gypsum in marine methane hydrate settings: Evidence from the northern South China Sea. *Deep-Sea Research: Part I, Oceanographic Research Papers*, v. 115, p. 210–220, doi:10.1016/j.dsr.2016.06.010.
- Liu, Q., Jackson, M. J., Yu, Y., Chen, F., Deng, C., and Zhu, R. (2004). Grain size distribution of pedogenic magnetic particles in Chinese loess/paleosols. *Geophys. Res. Lett.*, 31(22). . doi:10.1029/2004GL021090
- Liu, Q., Roberts, A. P., Larrasoaa, J. C., Banerjee, S. K., Guyodo, Y., Tauxe, L., et al. (2012). Environmental magnetism: principles and applications. *Rev. Geophys.* 50:RG4002. doi:10.1029/2012RG000393
- Maher, B. A. (1988). Magnetic properties of some synthetic sub-micron magnetites. *Geophys. J. Inter.*, 94(1), 83-96. doi:10.1111/j.1365-246X.1988.tb03429.x
- Maher, B. A., and Thompson, R. (Eds.). (1999). Quaternary climates, environments and magnetism. *Cambridge University Press*.
- Mazumdar A., Dewangan P., Peketi A., Gullapalli S., Kalpana M. S., Naik G. P., et al. (2019). The first record of active methane (cold) seep ecosystem associated with shallow methane hydrate from the Indian EEZ. *J. of Earth Sys. Sci.*, 128:18, doi:10.1007/s12040-018-1044-y
- Mazumdar, A., Dewangan, P., João, H.M., Peketi, A.,Khosla, V.R., Kocherla, M., et al., (2009). Evidence of paleo–cold seep activity from the Bay of Bengal, offshore India. *Geochem., Geophys., Geosys.*, 10Q06005. doi:10.1029/2008GC002337
- Mohamed, K. J., Rey, D., Rubio, B., Dekkers, M. J., Roberts, A. P., and Vilas, F. (2011). Onshore–offshore gradient in reductive early diagenesis in coastal marine sediments of the Ria de Vigo, Northwest Iberian Peninsula. *Cont. Shelf Res.*, 31(5), 433-447. doi:10.1016/j.csr.2010.06.006
- Moskowitz, B. M., Frankel, R. B., and Bazylinski, D. A. (1993). Rock magnetic criteria for the detection of biogenic magnetite. *Earth Planet. Sci. Lett.*, 120(3-4), 283–300. doi:10.1016/0012-821X(93)90245-5
- Musgrave, R. J., Bangs, N. L., Larrasoña, J. C., Gràcia, E., Hollamby, J. A., and Vega, M. E. (2006). Rise of the base of the gas hydrate zones since the last glacial recorded by rock magnetism. *Geology*, 34(2), 117–120. doi:10.1130/G22008.1
- Muxworthy, A. R., and Roberts, A. P., First-order reversal curve (FORC) diagrams, In: Gubbins, D and Herrero-Bervera, E, editor, *Encycl. Geomag. Paleomag.*, Springer, 2007, Pages: 266 – 272

- Muxworthy, A. R., and McClelland, E. (2000). Review of the low-temperature magnetic properties of magnetite from a rock magnetic perspective. *Geophys. J. Inter.*, 140(1), 101–114. doi:10.1046/j.1365-246x.2000.00999.x
- Muxworthy, A. R., & Evans, M. E. (2013). Micromagnetics and magnetomineralogy of ultrafine magnetite inclusions in the Modipe Gabbro. *Geochem., Geophys., Geosys.*, 14(4), 921-928. doi:10.1029/2012GC004445
- Neretin, L. N., Böttcher, M. E., Jørgensen, B. B., Volkov, I. I., Lüschen, H., and Hilgenfeldt, K. (2004). Pyritization processes and greigiteformation in the advancing sulfidization front in the upper Pleistocene sediments of the Black Sea 1. *Geochim. Cosmochim. Acta*, 68(9), 2081–2093. doi:10.1016/S0016-7037(03)00450-2
- Newell, A. J. (2005). A high-precision model of first-order reversal curve (FORC) functions for single-domain ferromagnets with uniaxial anisotropy. *Geochem., Geophys., Geosys.*, 6(5).https://doi.org/10.1029/2004GC000877
- Novosel, I., G. D. Spence, and R. D. Hyndman (2005), Reduced magnetization produced by increased methane flux at a gas hydrate vent, *Mar. Geol.*, 216(4), 265–274. doi:10.1016/j.margeo.2005.02.027.
- Novosel, N., Galić, S., Pajić, D., Zadro, K., and Babić, E. (2015). Enhancing Superconducting Properties of MgB₂ by Addition of Magnetic Particles. *J. Supercond.novel magnet.*, 28(2), 425-430. doi:10.1007/s10948-014-2807-6
- Nowaczyk, N. R. (2011). Dissolution of titanomagnetite and sulphidization in sediments from Lake Kinneret, Israel. *Geophys. J. Inter.*, 187(1), 34-44. doi:10.1111/j.1365-246X.2011.05120.x
- Nowaczyk, N. R., Arz, H. W., Frank, U., Kind, J., & Plessen, B. (2012). Dynamics of the Laschamp geomagnetic excursion from Black Sea sediments. *Earth Planet Sci. Lett.*, 351, 54-69. doi:10.1016/j.epsl.2012.06.050
- Ojha, P. S., and Dubey, M. (2006). Gaint hydrocarbon fields of offshore Krishna-Godavari Basin. *Petroview*, 1, 26-30.
- Özdemir, Ö., and Dunlop, D. J. (2010). Hallmarks of maghemitization in low-temperature remanence cycling of partially oxidized magnetite nanoparticles. *J. Geophys. Res. Solid Earth*, 115(B2). doi:10.1029/2009JB006756
- Özdemir, Ö., Dunlop, D. J., and Moskowitz, B. M. (1993). The effect of oxidation on the Verwey transition in magnetite. *Geophys. Res. Lett.*, 20(16), 1671-1674. doi:10.1029/93GL01483
- Özdemir, Ö., Dunlop, D. J., and Moskowitz, B. M. (2002). Changes in remanence, coercivity and domain state at low temperature in magnetite. *Earth Planet. Sci. Lett.*, 194(3-4), 343–358. doi:10.1016/S0012-821X(01)00562-3
- Pan, Y. X., Zhu, R. X., Banerjee, S. K., Gill, J., and Williams, Q. (2000). Rock magnetic properties related to thermal treatment of siderite: Behavior and interpretation. *J. Geophys. Res. Solid Earth*, 105, 783–794. doi:10.1029/1999JB900358

- Passier, H. D., De Lange, G. J., and Dekkers, M. J. (2001). Magnetic properties and geochemistry of the active oxidation front and the youngest sapropel in the eastern Mediterranean Sea. *Geophys. J. Inter.*, 145(3), 604–614. doi:10.1046/j.0956-540x.2001.01394.x
- Passier, H. F., and Dekkers, M. J. (2002). Iron oxide formation in the active oxidation front above sapropel S1 in the eastern Mediterranean Sea as derived from low-temperature magnetism. *Geophys. J. Inter.*, 150(1), 230–240. doi:10.1046/j.1365-246X.2002.01704.x
- Peters, C., and Dekkers, M. J. (2003). Selected room temperature magnetic parameters as a function of mineralogy, concentration and grain size. *Phys. Chem. Earth, Parts A/B/C*, 28(16-19), 659-667. doi:10.1016/S1474-7065(03)00120-7
- Petersen, N., T. Von Dobeneck, and H. Vali (1986). Fossil bacterial magnetite in deep-sea sediments from the South Atlantic Ocean, *Nature*, 320, 611–615. doi:10.1038/320611a0
- Pike, C.R., Roberts, A.P., and Verosub, K.L. (1999) Characterizing interactions in fine magnetic particle systems using first order reversal curves. *J. Appl. Phys.* 85(9):6660–6667. doi:10.1063/1.370176
- Poulton, S. W., Krom, M. D., and Raiswell, R. (2004). A revised scheme for the reactivity of iron (oxyhydr) oxide minerals towards dissolved sulfide. *Geochim. Cosmochim. Acta*, 68(18), 3703-3715. doi:10.1016/j.gca.2004.03.012.
- Prabhakar, K.N., and Zutshi, P.L. (1993). Evolution of southern part of Indian East Coast basin. *J. Geol. Soc. Ind.* 41:215–230
- Prozorov, T., Mallapragada, S. K., Narasimhan, B., Wang, L., Palo, P., Nilsen-Hamilton, et al. (2007). Protein-mediated synthesis of uniform super paramagnetic magnetite nanocrystals. *Advanced Functional Materials*, 17(6), 951-957. doi:10.1002/adfm.200600448
- Ramesh, R., and Subramanian, V. (1988), Temporal, spatial and size variation in the sediment transport in the Krishna River basin, India, *J. Hydrol.*, 98, 53–65.
- Ramana, M. V., Ramprasad, T., Kamesh Raju, K. A., & Desa, M. (2007). Occurrence of gas hydrates along the continental margins of India, particularly the Krishna-Godavari off shore basin. *Int. J. Env. Stu.*, 64(6), 675–693. doi:10.1080/00207230701476321
- Ramprasad, T., Dewangan, P., Ramana, M.V., Mazumdar, A., Karisiddaiah, S.M., Ramya, E.R., et al. (2011). Evidence of slumping/sliding in Krishna–Godavari offshore basin due to gas/fluid movements. *Mar. Petrol. Geol.* 28, 1806–1816. doi:10.1016/j.marpetgeo.2011.02.007
- Rao, V. P. (1991). Clay mineral distribution in the continental shelf sediments from Krishna to Ganges river mouth, east coast of India. *Ind. J. Mar. Sci.*, 20, 7–12.
- Reidinger, N., Pfeifer, K., Kasten, S., Garming, J. F. L., Vogt, C., and Hensen C. (2005). Diagenetic alteration of magnetic signals by anaerobic oxidation of methane related to a change in sedimentation rate, *Geochim. Cosmochim. Acta*, 69, 4117–4126, doi:10.1016/j.gca.2005.02.004.
- Reilly, B. T., McCormick, M. L., Brachfeld, S. A., and Haley, B. A. (2020). Authigenic ferrimagnetic iron sulfide preservation due to non-steady state diagenesis: A perspective from Perseverance Drift, North western Weddell Sea. *Geochem., Geophys., Geosys.*, e2020GC009380. doi:10.1029/2020GC009380

- Riedel, M., Spence, G. D., Chapman, N. R., and Hyndman, R. D. (2002). Seismic investigations of a vent field associated with gas hydrates, offshore Vancouver Island. *J. Geophys. Res. Solid Earth*, 107(B9), EPM-5. doi:10.1029/2001JB000269
- Reidinger, N., Pfeifer, K., Kasten, S., Garming, J. F. L., Vogt, C., and Hensen C. (2005). Diagenetic alteration of magnetic signals by anaerobic oxidation of methane related to a change in sedimentation rate, *Geochim. Cosmochim. Acta*, 69, 4117–4126, doi:10.1016/j.gca.2005.02.004.
- Riedinger, N., Formolo, M. J., Lyons, T. W., Henkel, S., Beck, A., and Kasten, S. (2014). An inorganic geochemical argument for coupled anaerobic oxidation of methane and iron reduction in marine sediments. *Geobiology*, 12(2), 172-181. doi:10.1111/gbi.12077
- Roberts, A. P. (1995). Tectonic rotation about the termination of a major strike-slip fault, Marlborough Fault System, New Zealand. *Geophys. res. lett.*, 22(3), 187-190. doi:10.1029/94GL02582
- Roberts, A. P. (2015). Magnetic mineral diagenesis. *Earth-Sci. Rev.*, 151, 1–47. doi:10.1016/j.earscirev.2015.09.010
- Roberts, A. P., Almeida, T. P., Church, N. S., Harrison, R. J., Heslop, D., Li, Y., et al. (2017). Resolving the origin of pseudo-single domain magnetic behavior. *J. Geophys. Res. Solid Earth*, 122, 9534–9558. doi:10.1002/2017JB014860
- Roberts, A. P., and Weaver, R. (2005). Multiple mechanisms of remagnetization involving sedimentary greigite (Fe₃S₄). *Earth Planet. Sci. Lett.*, 231, 263–277. doi:10.1016/j.epsl.2004.11.024
- Roberts, A. P., Chang, L., Rowan, C. J., Horng, C. S., and Florindo, F. (2011). Magnetic properties of sedimentary greigite (Fe₃S₄): An update. *Rev. Geophys.*, 49, RG1002. doi:10.1029/2010RG000336
- Roberts, A. P., Jiang, W. T., Florindo, F., Horng, C. S., and Laj, C. (2005). Assessing the timing of greigite formation and the reliability of the Upper Olduvai polarity transition record from the Crostolo River, Italy. *Geophys. Res. Lett.*, 32(5). doi:10.1029/2004GL022137
- Roberts, A. P., Zhao, X., Harrison, R. J., Heslop, D., Muxworthy, A. R., Rowan, C. J., et al. (2018). Signatures of reductive magnetic mineral diagenesis from unmixing of first order reversal curves. *J. Geophys. Res. Solid Earth*, 123, 4500–4522. doi:10.1029/2018JB015706
- Roberts, A. P., Zhao, X., Heslop, D., Abrajevitch, A., Chen, Y. H., Hu, P., et al. (2020). Hematite (α -Fe₂O₃) quantification in sedimentary magnetism: limitations of existing proxies and ways forward. *Geoscience Letters*, 7(1), 1-11. doi:10.1186/s40562-020-00157-5
- Rodelli, D., Jovane, L., Giorgioni, M., Rego, E. S., Cornaggia, F., Benites, M., Cedraz, P.; et al. (2019). Diagenetic fate of biogenic soft and hard magnetite in chemically stratified sedimentary environments of Mamanguá Ría, Brazil. *J. Geophys. Res. Solid Earth*, 124(3), 2313-2330. doi: 10.1029/2018JB016576
- Rodelli, D., Jovane, L., Roberts, A. P., Cypriano, J., Abreu, F., Lins, U. (2018). Fingerprints of partial oxidation of biogenic magnetite from cultivated and natural marine magnetotactic bacteria using synchrotron radiation. *Environmental microbiology reports*, 10(3), 337-343. doi: 10.1111/1758-2229.12644

- Römer, M., Sahling, H., Pape, T., dos Santos Ferreira, C., Wenzhöfer, F., Boetius, A., et al. (2014). Methane fluxes and carbonate deposits at a cold seep area of the Central Nile Deep Sea Fan, Eastern Mediterranean Sea. *Mar. Geol.*, 347, 27-42. doi:10.1016/j.margeo.2013.10.011
- Rowan, C. J., and Roberts, A. P. (2006). Magnetite dissolution, diachronous greigite formation, and secondary magnetizations from pyrite oxidation: Unravelling complex magnetizations in Neogene marine sediments from New Zealand. *Earth Planet. Sci. Lett.*, 241(1-2), 119–137. doi:10.1016/j.epsl.2005.10.017
- Rowan, C. J., Roberts, A. P., and Broadbent, T. (2009). Reductive diagenesis, magnetite dissolution, greigite growth and paleomagnetic smoothing in marine sediments: A new view. *Earth Planet. Sci. Lett.*, 277(1-2), 223–235. doi:10.1016/j.epsl.2008.10.016
- Sagnotti, L., and Winkler, A. (1999). Rock magnetism and palaeomagnetism of greigite-bearing mudstones in the Italian peninsula. *Earth Planet. Sci. Lett.*, 165, 67–80. doi: 10.1016/s0012-821x(98)00248-9
- Sagnotti, L., Cascella, A., Ciaranfi, N., Macrì, P., Maiorano, P., Marino, M., et al. (2010). Rock magnetism and palaeomagnetism of the Montalbano Jonico section (Italy): evidence for late diagenetic growth of greigite and implications for magnetostratigraphy. *Geophys. J. Int.*, 180(3), 1049-1066. doi:10.1111/j.1365-246X.2009.04480.x
- Sagnotti, L., Roberts, A. P., Weaver, R., Verosub, K. L., Florindo, F., Pike, C. R., et al. (2005). Apparent magnetic polarity reversals due to remagnetization resulting from late diagenetic growth of greigite from siderite. *Geophys J Int*, 160(1), 89–100. doi:10.1111/j.1365-246X.2005.02485.x
- Sangode, S. J., Sinha, R., Phartiyal, B., Chauhan, O. S., Mazari, R. K., Bagati, T. N., et al. (2007). Environmental magnetic studies on some quaternary sediments of varied depositional settings in the Indian sub-continent. *Quat. Int.*, 159, 102–118. doi:10.1016/j.quaint.2006.08.015
- Sangode, S. J., Suresh, N., and Bagati, T. N. (2001). Godavari source in the Bengal fan sediments: Results from magnetic susceptibility dispersal pattern. *Current Science*, 660–664.
- Shankar, U., and Riedel, M. (2010). Seismic and heat flow constraints from the gas hydrate system in the Krishna-Godavari basin, India. *Mar. Geol.*, 276(1–4), 1–13. doi:10.1016/j.margeo.2010.06.006
- Simonetti, A., Knapp, J. H., Sleeper, K., Lutken, C. B., Macelloni, L., and Knapp, C. C. (2013). Spatial distribution of gas hydrates from higher resolution seismic and core data, Woolsey Mound, Northern Gulf of Mexico, *Mar. Petrol. Geol.*, 44, 21–33, doi:10.1016/j.marpetgeo.2013.04.004.
- Singhroha, S., Bünz, S., Plaza-Faverola, A., and Chand, S. (2020). Detection of Gas Hydrates in Faults Using Azimuthal Seismic Velocity Analysis, Vestnesa Ridge, W-Svalbard Margin. . *J. Geophys. Res. Solid Earth*, 125(2), e2019JB017949. doi:10.1029/2019JB017949
- Snowball, I., and Thompson, R. (1990). A stable chemical remanence in Holocene sediments. . *J. Geophys. Res. Solid Earth*, 95(B4), 4471-4479. doi:10.1029/JB095iB04p04471
- Suess, E. (2014). Marine cold seeps and their manifestations: geological control, biogeochemical criteria and environmental conditions. *Int. J. Earth Sci.*, 103(7), 1889-1916. doi:10.1007/s00531-014-1010-0

- Sztybor, K., and Rasmussen, T. L. (2017). Diagenetic disturbances of marine sedimentary records from methane-influenced environments in the Fram Strait as indications of variation in seep intensity during the last 35 000 years. *Boreas*, 46(2), 212-228. doi:10.1111/bor.12202
- Tarduno, J. A. (1995). Superparamagnetism and reduction diagenesis in pelagic sediments: enhancement or depletion? *Geophys. Res. Lett.*, 22(11), 1337-1340. doi:10.1029/95GL00888
- Tarduno, J. A., Cottrell, R. D., and Smirnov, A. V. (2006). The paleomagnetism of single silicate crystals: Recording geomagnetic field strength during mixed polarity intervals, super chrons, and inner core growth. *Rev. Geophys.*, 44(1). doi:10.1029/2005RG000189
- Thompson, R., and Oldfield, F. (1986). Environmental magnetism, (p. 227). London: Allen and Unwin.
- Usapkar, A., Dewangan, P., Kocherla, M., Ramprasad, T., Mazumdar, A., and Ramana, M. V. (2014). Enhanced methane flux event and sediment dispersal pattern in the Krishna–Godavari offshore basin: Evidences from rock magnetic techniques. *Mar. Petrol. Geol.*, 58, 461–475 doi:10.1016/j.marpetgeo.2014.08.008
- Valdez-Grijalva, M. A., Nagy, L., Muxworthy, A. R., Williams, W., Roberts, A. P., Heslop, D. (2020). Micromagnetic simulations of first-order reversal curve (FORC) diagrams of framboidal greigite. *Geophysical Journal International*, 222(2), 1126-1134. doi:10.1093/gji/ggaa241
- Verwey, E. J. W. (1939). Electronic conduction of magnetite (Fe₃O₄) and its transition point at low temperatures. *Nature*, 144(3642), 327. doi:10.1038/144327b0
- Verwey, E. J. W. (1947). Theory of the stability of lyophobic colloids. *J. Phys. Chem.*, 51(3), 631-636. doi:10.1021/j150453a001
- Wang, X., Liu, B., Qian, J., Zhang, X., Guo, Y., Su, P. et al. (2018). Geophysical evidence for gas hydrate accumulation related to methane seepage in the Taixinan Basin, South China Sea. *J.f Asian Earth Sci.*, 168, 27-37. doi:10.1016/j.jseaes.2017.11.011
- Wenau, S., Spiess, V., Pape, T., and Fekete, N. (2015). Cold seeps at the salt front in the Lower Congo Basin II: The impact of spatial and temporal evolution of salt-tectonics on hydrocarbon seepage. *Mar. Petrol. Geol.*, 67, 880-893. doi:10.1016/j.marpetgeo.2014.09.021
- Yamazaki, T., Abdeldayem, A. L. and Ikehara, K. (2003), Rock-magnetic changes with reduction diagenesis in Japan Sea sediments and preservation of geomagnetic secular variation in inclination during the last 30,000 years, *Earth Planet Space*, 55, 327–340.
- Yamamoto, Y., Chiyonobu, S., Kanamatsu, T., Ahagon, N., Aoike, K., Kamiya, N., & Kinoshita, M. (2018). Repeated large-scale mass transport deposits and consequent rapid sedimentation in the western part of the Bay of Bengal, India. *Geol Society, London, Special Publications*. In G. (Vol. 477SP477–12). doi:10.1144/SP477.12
- Yao, H., Hong, W. L., Panieri, G., Sauer, S., Torres, M. E., Lehmann, M. F., et al. (2019). Fracture-controlled fluid transport supports microbial methane-oxidizing communities at Vestnesa Ridge. Yao, H. (2020). Reconstruction of past and present methane emission in the Arctic cold seeps using biogeochemical proxies. (Doctoral thesis).

Figure-1

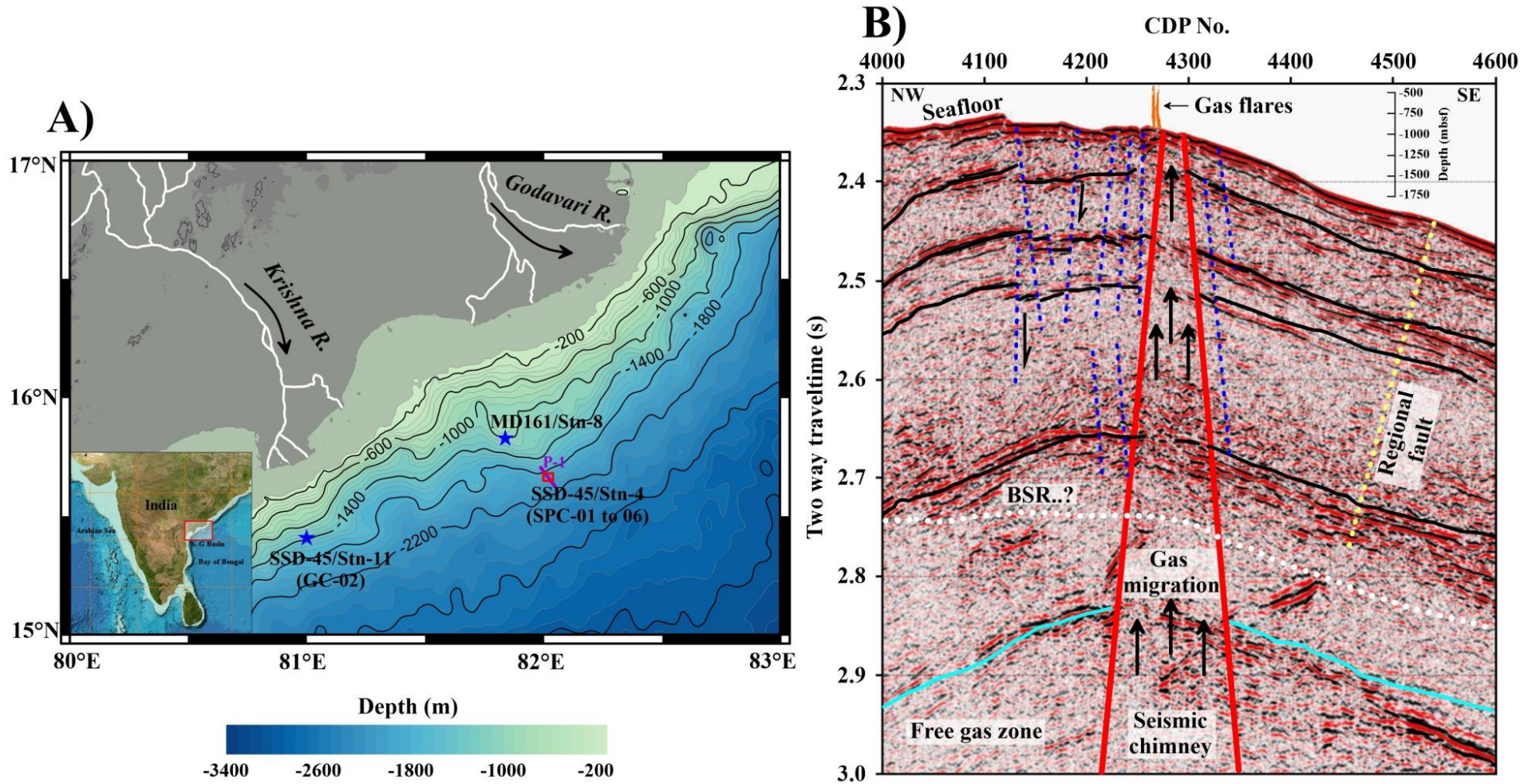


Figure-2

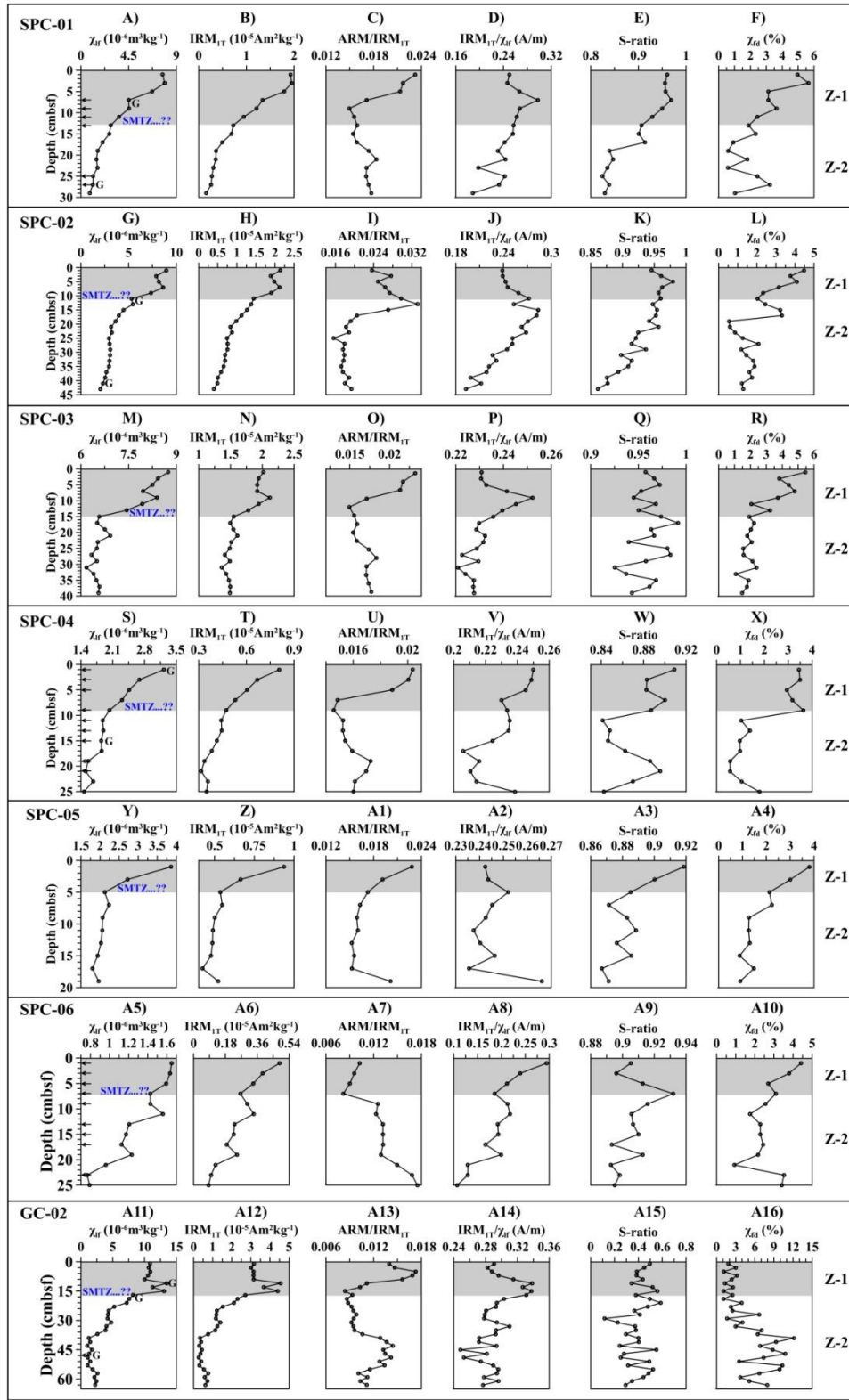


Figure-3

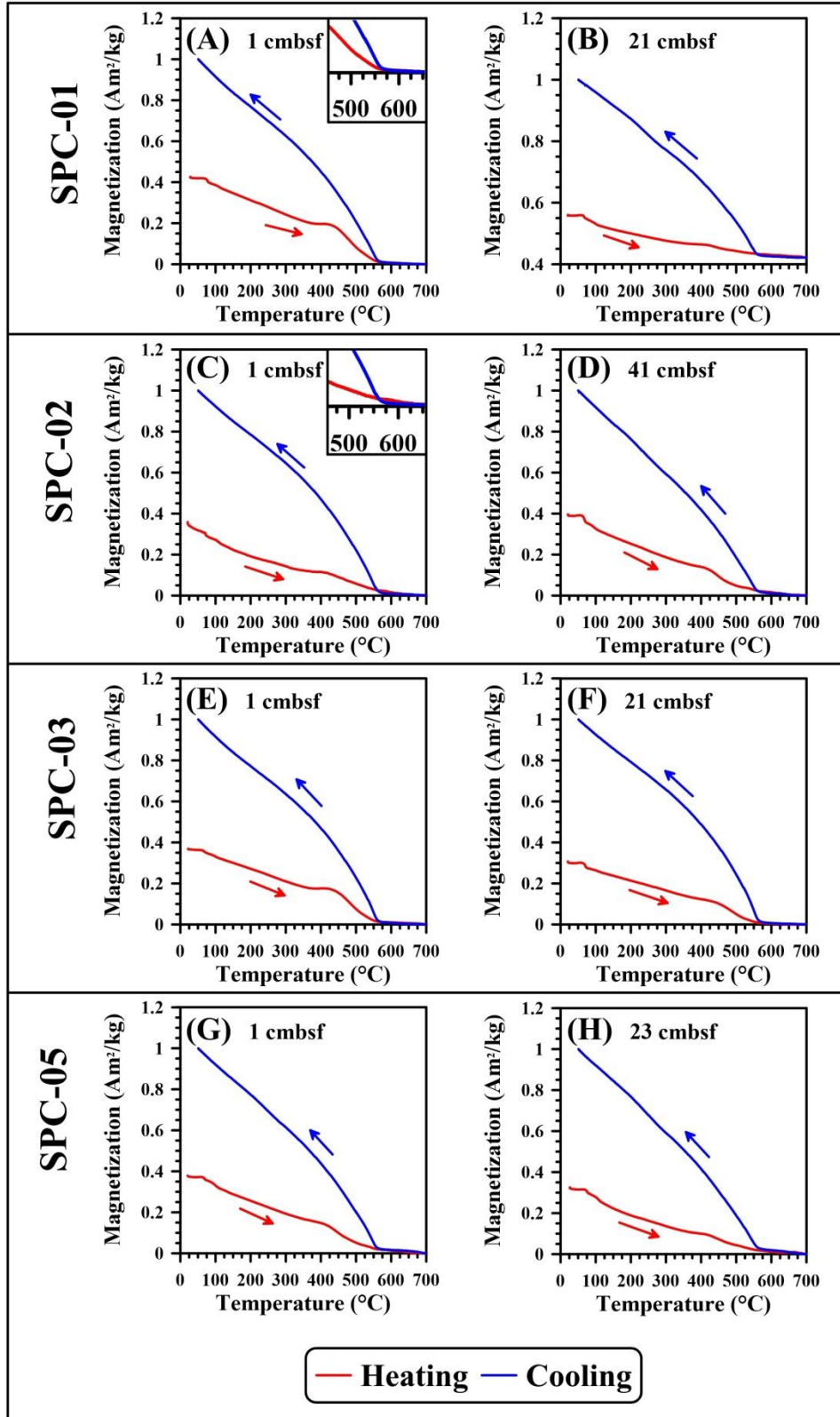


Figure-4

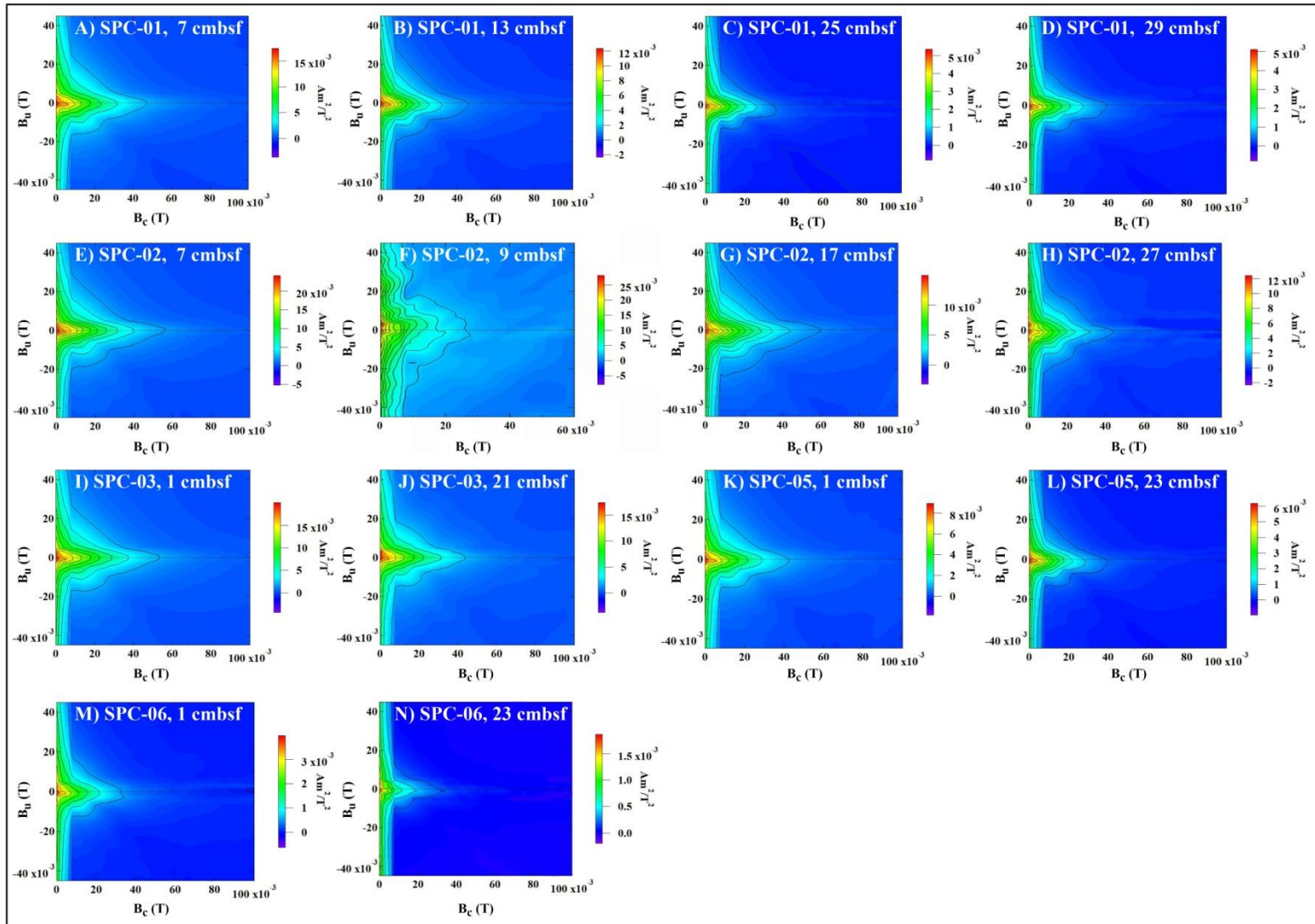


Figure-5

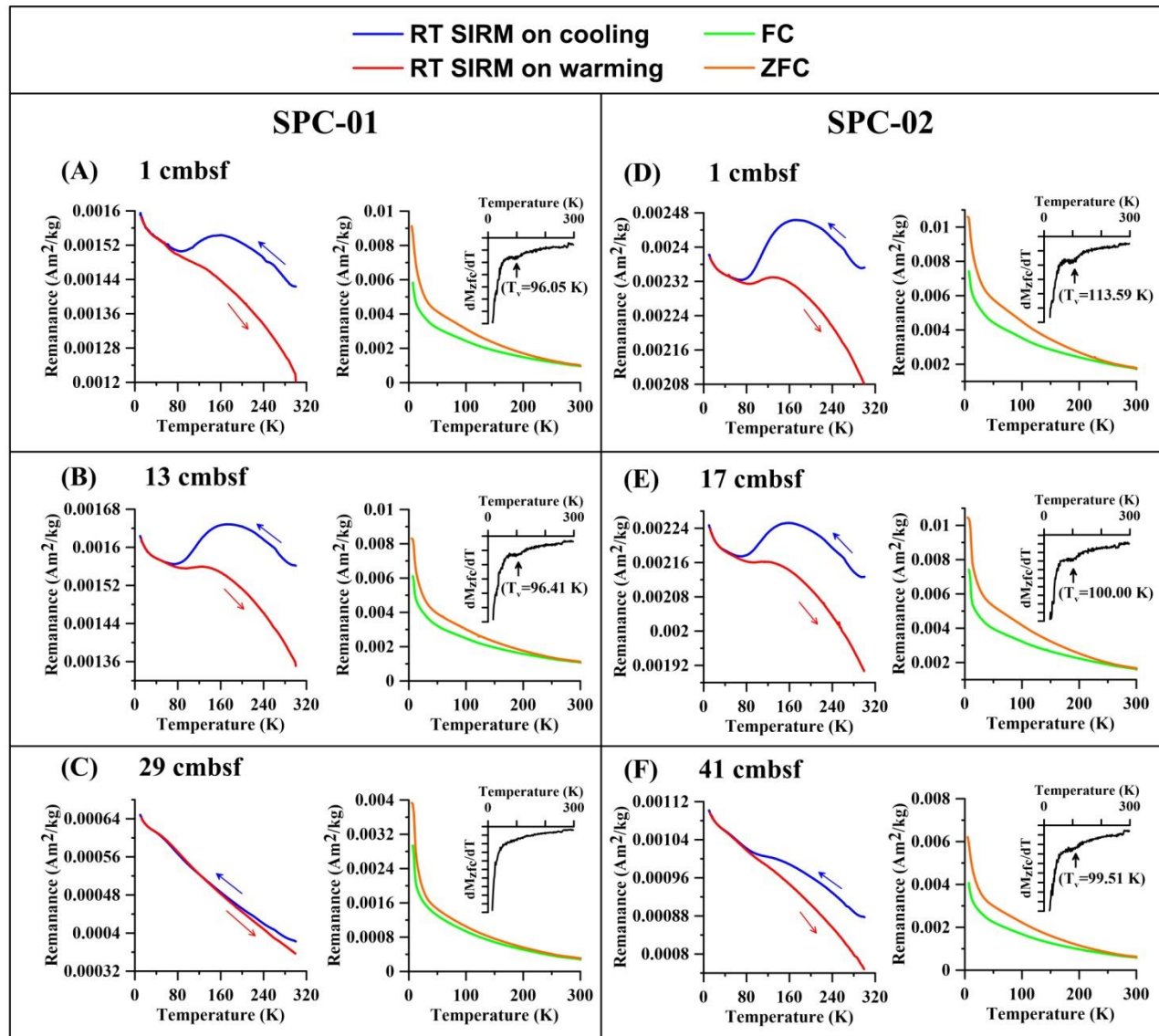


Figure-6

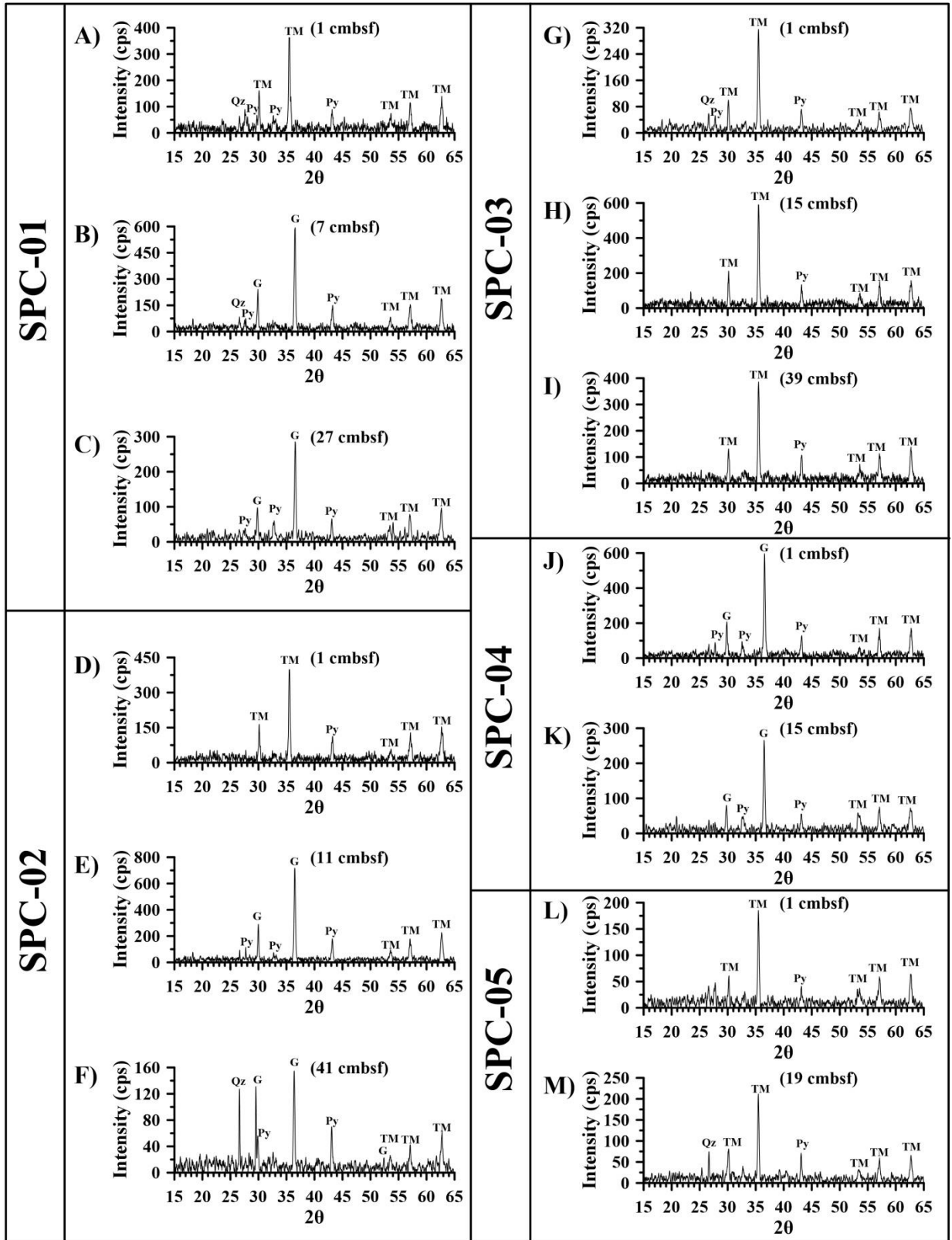


Figure-7

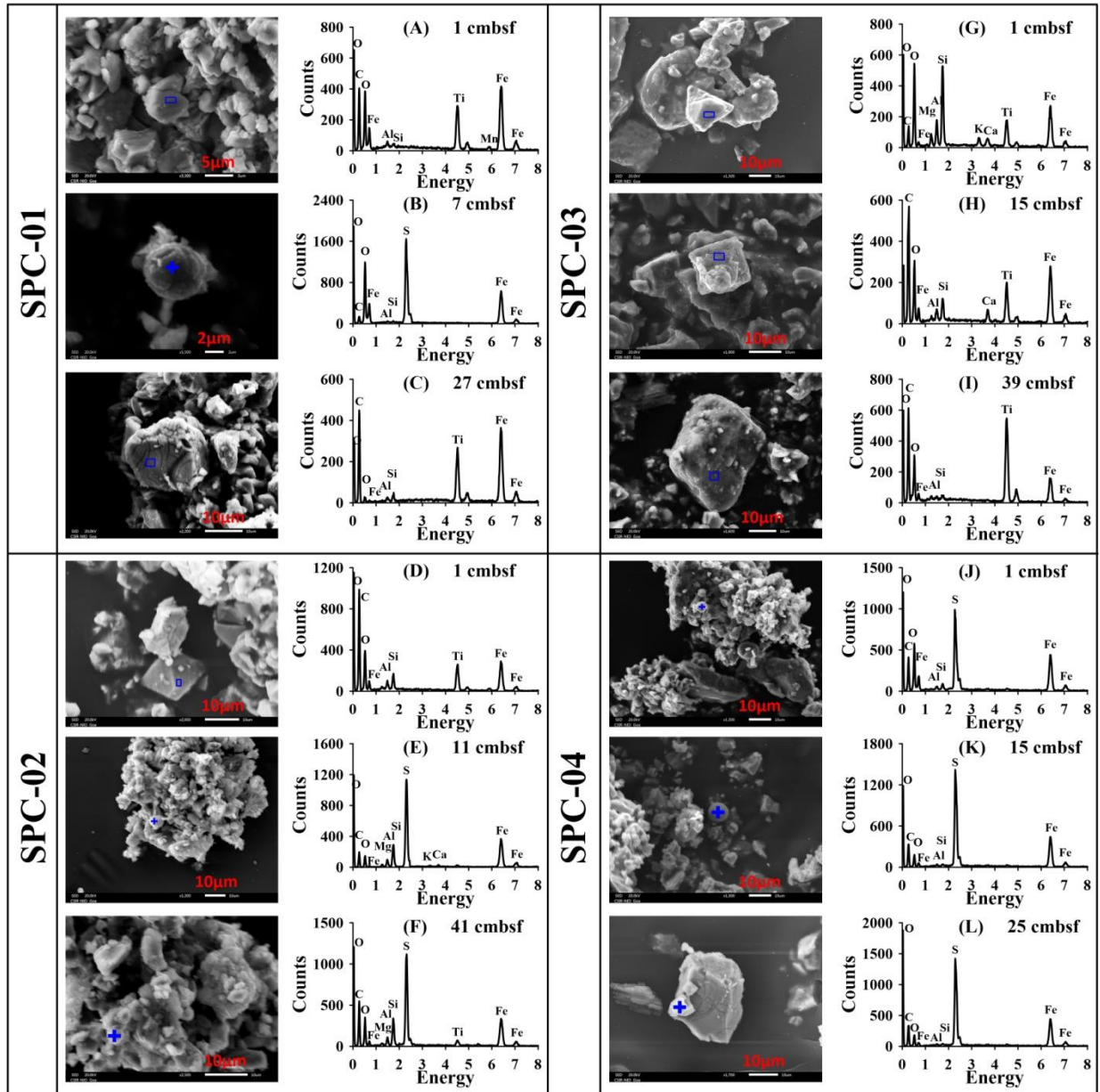


Figure-8

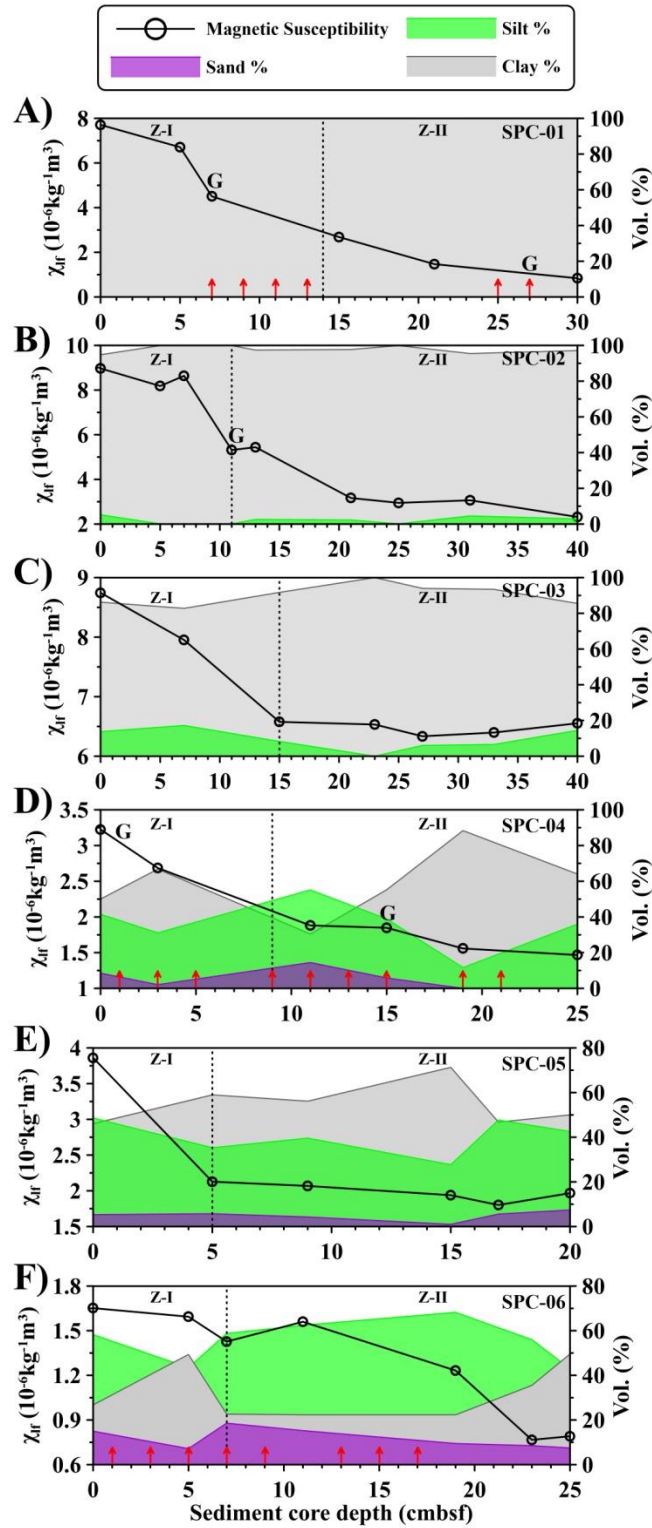


Figure-9

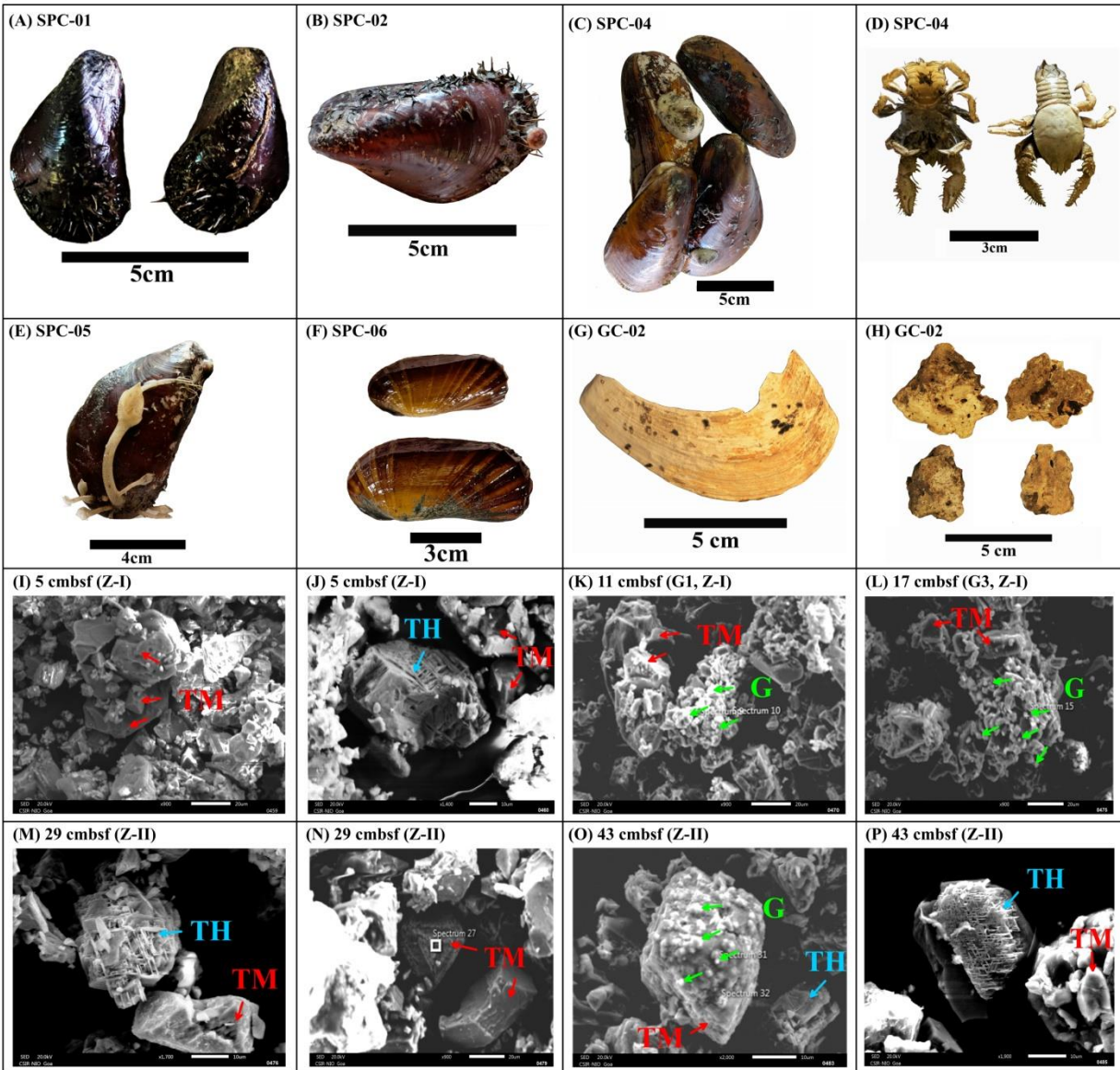


Figure-10

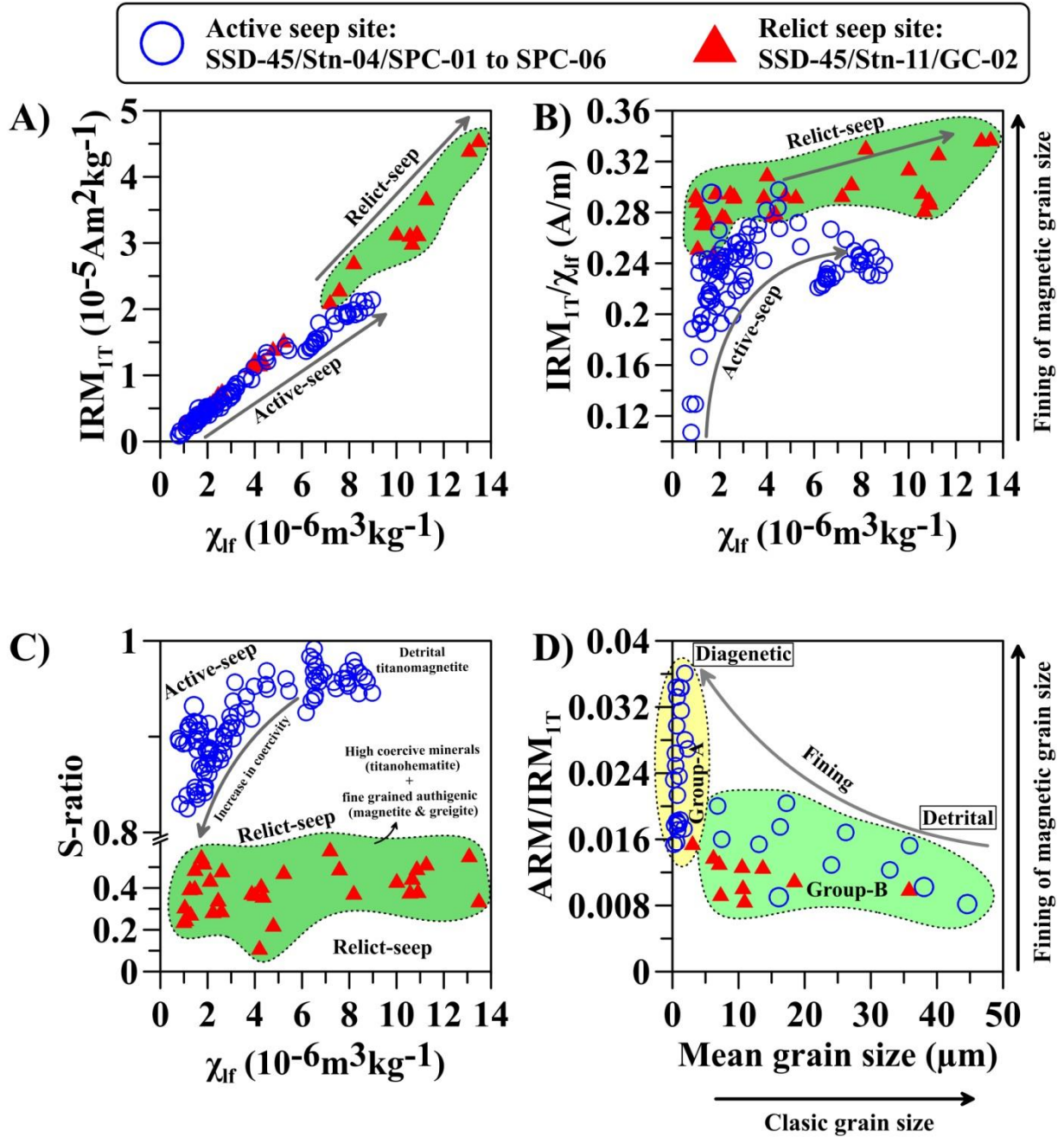


Figure-11

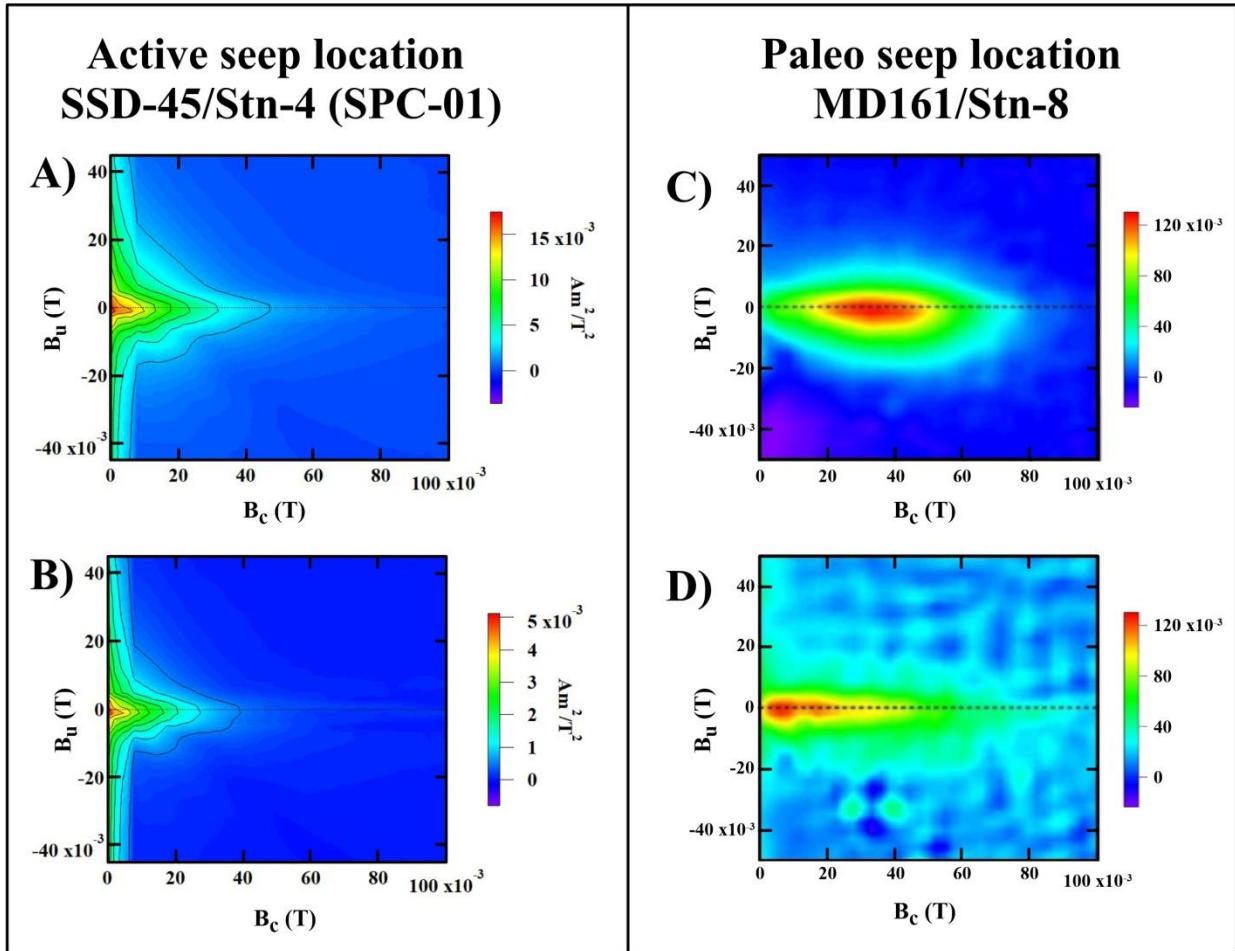


Figure-12

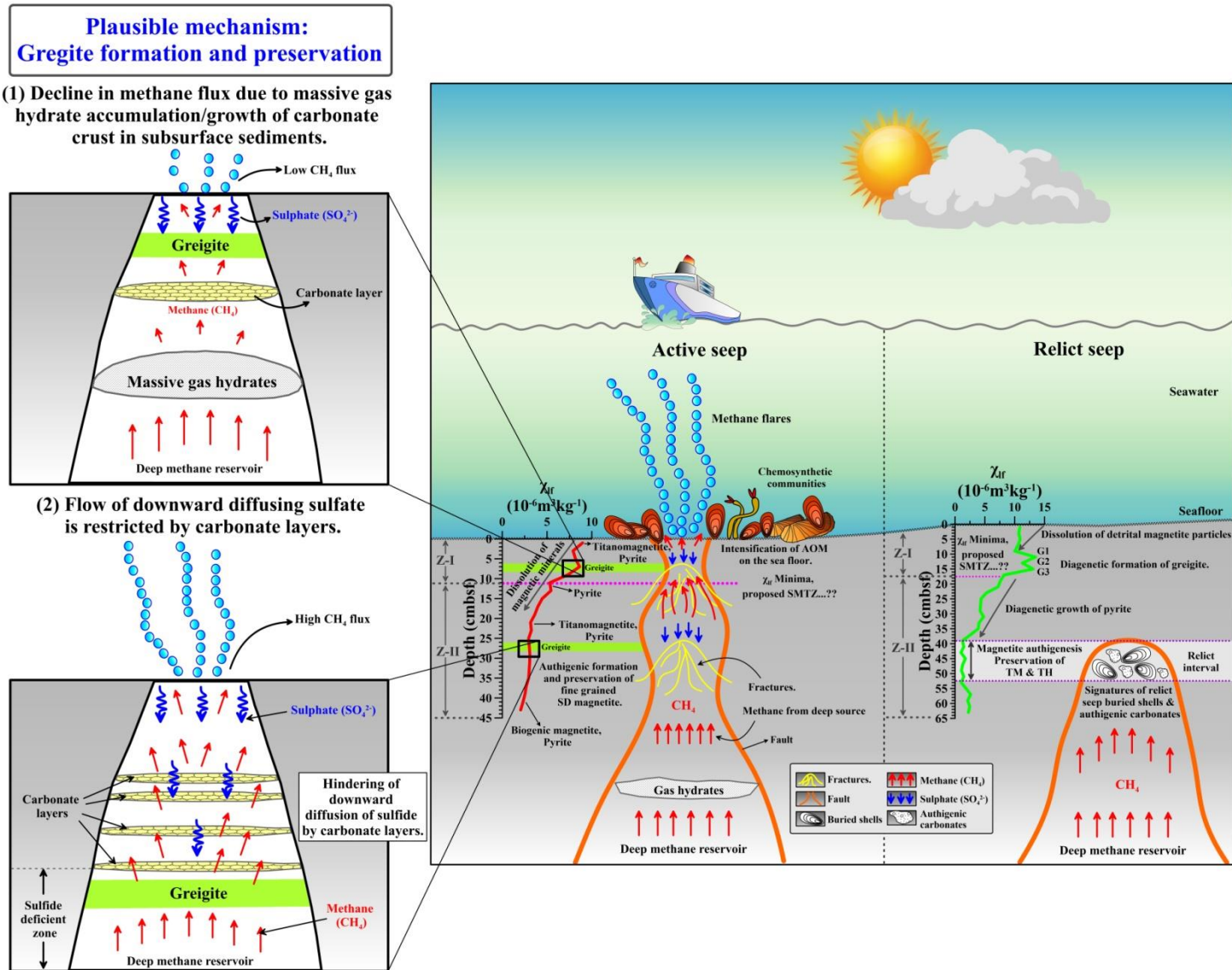


Figure-13

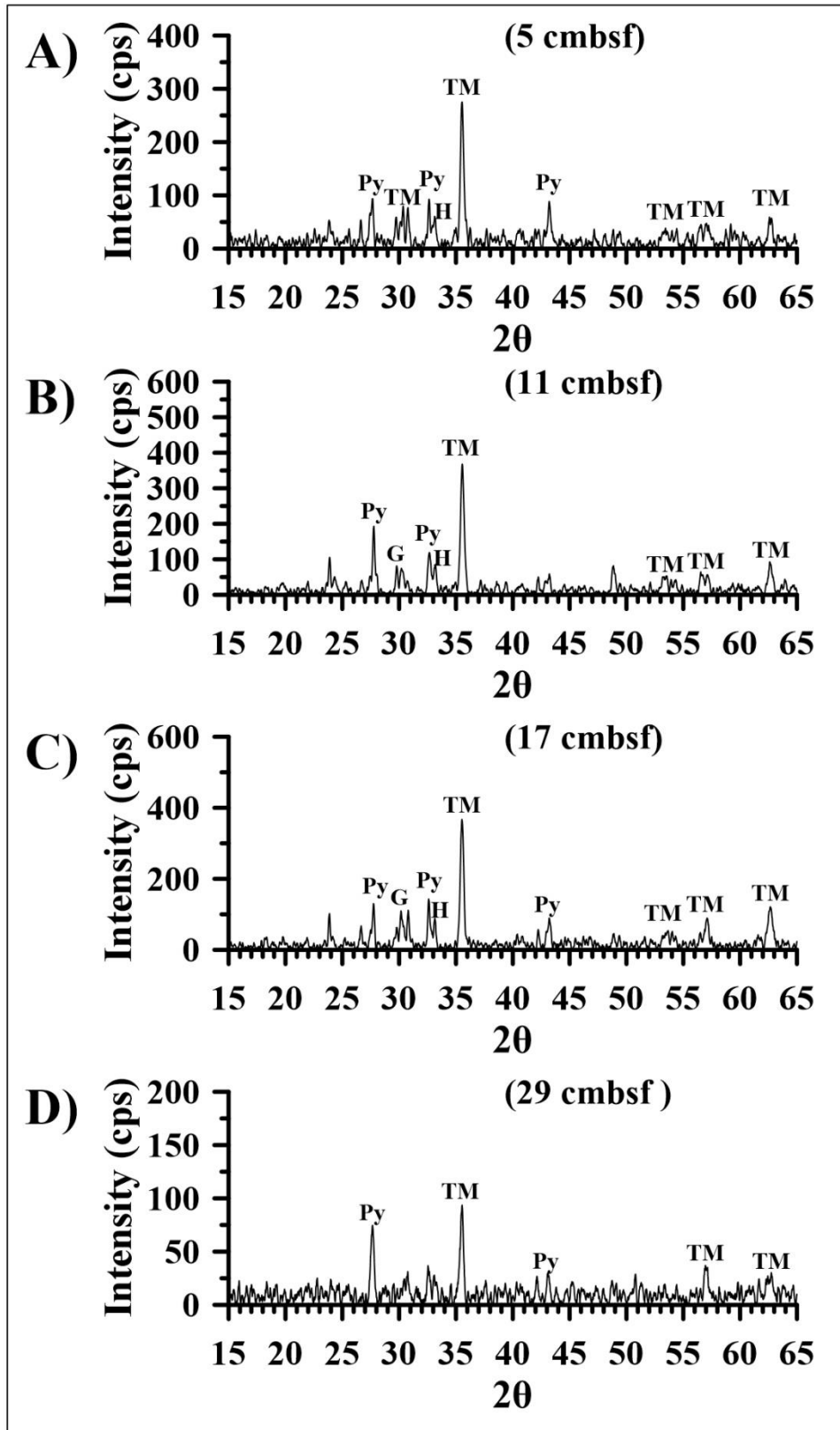


Figure-14

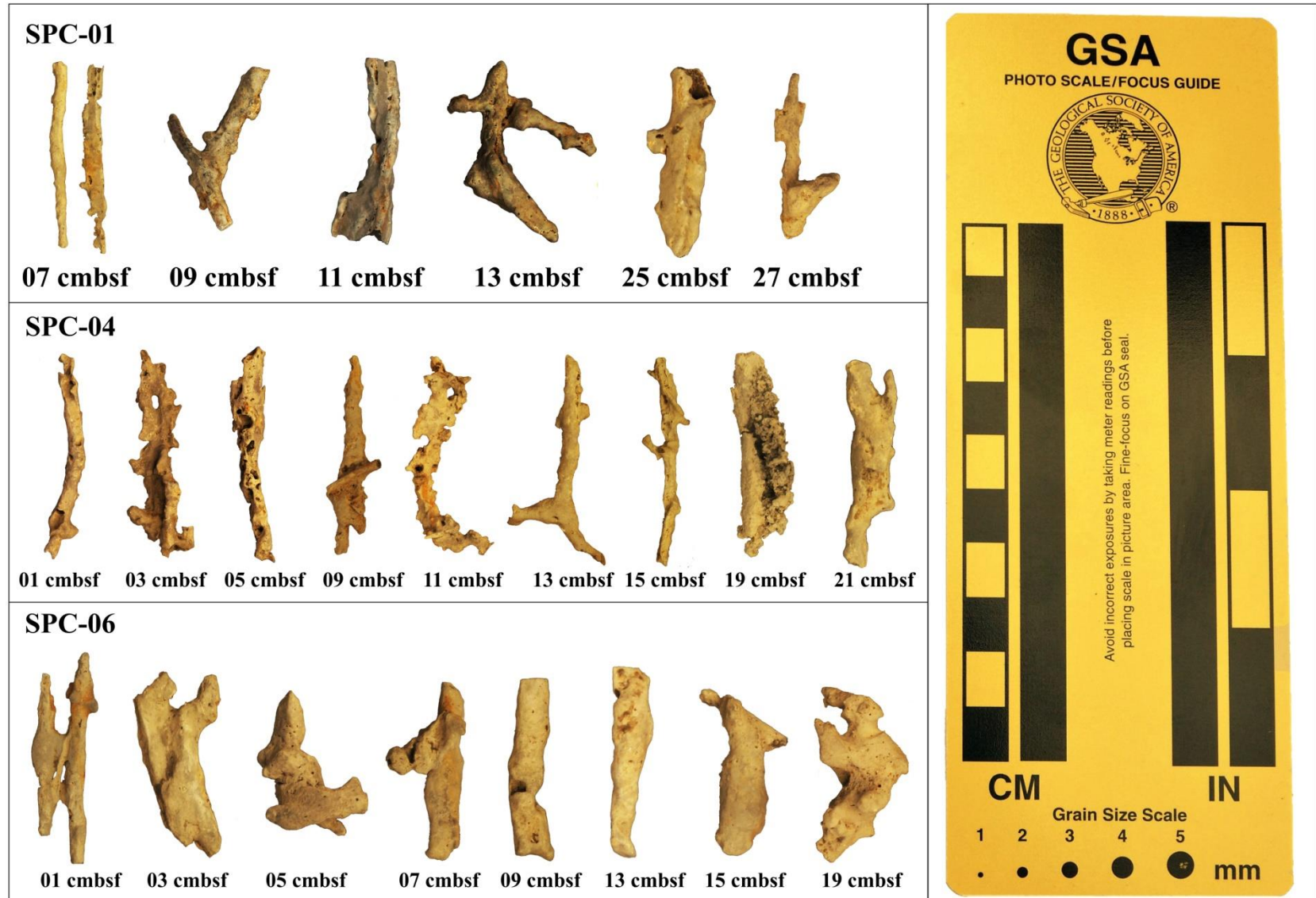


Table 1. Information of spade sediment cores retrieved from an active seep site in the Krishna-Godavari (K-G) basin, Bay of Bengal.

Core No.	Location		Water depth (m)	Core recovery (cm)	Core Description
	Lat. (°N)	Long. (°E)			
SPC-01	15°42.9986	82°04.0154	1755.0	30	0-4 cmbsf, light gray sediment; 4-30cmbsf homogeneous deep black sediment; live <i>Bathymodiolus</i> sp. found on surface of the spade core.
SPC-02	15°43.0058	82°04.0787	1756.5	43	0-18cmbsf, light gray sediments; 18-43cmbsf deep black sediments; live <i>Bathymodiolus</i> sp. found on surface of the spade core.
SPC-03	15°43.0055	82°04.0791	1754.0	40	0-40cmbsf, homogenous light gray sediments throughout the core; chemosynthetic community were not found in this core.
SPC-04	15°42.9098	82°03.9825	1756.4	25	0-25cmbsf, homogenous deep black sediments throughout the core; strong H ₂ S smell during sub-sampling the core; live <i>Bathymodiolus</i> sp. and squat lobsters were found in this spade core.
SPC-05	15°43.0411	82°04.0599	1750.0	20	0-20cmbsf, homogenous deep black sediments throughout the core; moderate H ₂ S smell during sub-sampling the core; live <i>Bathymodiolus</i> sp. found in this spade core.
SPC-06	15°42.0991	82°04.0006	1754.0	25	0-25cmbsf, homogenous deep black sediments throughout the core; moderate H ₂ S smell during sub-sampling the core; live <i>Bathymodiolus</i> sp. and <i>Acharax</i> sp. were found in this spade core..
GC-02	15°24.1603	81°00.3078	1354.0	63	0-45cmbsf, homogenous deep black sediments; 45-63cmbsf homogenous gray sediments; buried <i>Calypptogena</i> sp. and authigenic carbonates were found at 48cmbsf in this gravity core.